Atmos. Meas. Tech. Discuss., 4, 1303–1370, 2011
www.atmos-meas-tech-discuss.net/4/1303/2011/
doi:10.5194/amtd-4-1303-2011

Atmospheric Measurement Techniques Discussions

Measuring the 3-D wind vector with a weight-shift microlight aircraft

S. Metzger[1,2], W. Junkermann[1], K. Butterbach-Bahl[1], H. P. Schmid[1], and T. Foken[3]

[1]Karlsruhe Institute of Technology, Institute for Meteorology and Climate Research, Garmisch-Partenkirchen, Germany
[2]Chinese Academy of Sciences, Institute of Atmospheric Physics, Beijing, China
[3]University of Bayreuth, Department of Micrometeorology, Bayreuth, Germany

Received: 20 January 2011 – Accepted: 11 February 2011 – Published: 28 February 2011

Correspondence to: W. Junkermann (wolfgang.junkermann@kit.edu)

Published by Copernicus Publications on behalf of the European Geosciences Union.

Abstract

This study investigates whether the 3-D wind vector can be measured reliably from a highly transportable and low-cost weight-shift microlight aircraft. Therefore we draw up a transferable procedure to accommodate flow distortion originating from the aircraft body and -wing. This procedure consists of the analysis of aircraft dynamics and seven successive calibration steps. For our aircraft the horizontal wind components receive their greatest single amendment (14%, relative to the initial uncertainty) from the correction of flow distortion magnitude in the dynamic pressure computation. Conversely the vertical wind component is most of all improved (31%) by subsequent steps considering the 3-D flow distortion distribution in the flow angle computations. Therein the influences of the aircraft's aeroelastic wing (53%), as well as sudden changes in wing loading (16%) are considered by using the measured lift coefficient as explanatory variable. Three independent lines of analysis are used to evaluate the quality of the wind measurement: (a) A wind tunnel study in combination with the propagation of sensor uncertainties defines the systems input uncertainty to $\approx 0.6\,\mathrm{m\,s^{-1}}$ at the extremes of a 95% confidence interval. (b) During severe vertical flight manoeuvres the deviation range of the vertical wind component does not exceed $0.3\,\mathrm{m\,s^{-1}}$. (c) The comparison with ground based wind measurements yields an overall operational uncertainty (root mean square deviation) of $\approx 0.4\,\mathrm{m\,s^{-1}}$ for the horizontal and $\approx 0.3\,\mathrm{m\,s^{-1}}$ for the vertical wind components. No conclusive dependence of the uncertainty on the wind magnitude ($<8\,\mathrm{m\,s^{-1}}$) or true airspeed (ranging from 23–30 $\mathrm{m\,s^{-1}}$) is found. Hence our analysis provides the necessary basis to study the wind measurement precision and spectral quality, which is prerequisite for reliable eddy-covariance flux measurements.

1 Introduction

In environmental science, spatial representativeness of measurements is a general problem. The limited coverage of ground based measurements requires strategies to better understand spatial patterns (e.g., Baldocchi et al., 2001; Beyrich et al., 2006). Here airborne measurements are capable of supplementing and extrapolating ground based information (e.g., Lenschow, 1986; Desjardins et al., 1997; Mauder et al., 2008). However, to date manned platforms, such as fixed-wing aircraft (FWA, see Appendix C for a summary of all notation) and helicopters, are expensive to operate. Furthermore, their application is often not possible in settings such as remote areas beyond the range of an airfield. Here small size unmanned aerial vehicles are of use. These allow the measurement of a limited range of variables, such as temperature, humidity and wind vector (e.g., Egger et al., 2002; Hobbs et al., 2002; van den Kroonenberg et al., 2008). However due to payload constraints, they do not allow a comprehensive sensor package. A weight-shift microlight aircraft (WSMA) may provide a low-cost and easily transportable alternative, which also places a minimal demand on infrastructure in the measurement location. After successfully applying a WSMA to aerosol and radiation transfer studies (e.g., Junkermann, 2001, 2005), the possibility of 3-D wind vector measurement from WSMA shall be explored. The underlying motivation is to work towards eddy-covariance (EC) flux measurements in the atmospheric boundary layer (ABL).

The determination of the 3-D wind vector from an airborne, i.e. moving platform, requires a high degree of sophistication. Specially designed probes enable the measurement of the 3-D turbulent wind field with respect to the aircraft (e.g., Brown et al., 1983; Crawford and Dobosy, 1992). At the same time the aircraft's movement with respect to the earth must be captured (e.g., Lenschow, 1986; Kalogiros and Wang, 2002a). A total of 15 measured quantities are involved in the computation of the 3-D wind vector (Appendix A), and consequently a similar number of potential uncertainty sources need to be considered. Furthermore, flow distortion by the aircraft itself can affect the measurement (e.g., Crawford et al., 1996; Kalogiros and Wang, 2002b; Garman et al., 2008). This complexity led to a number of quantitative uncertainty assessments of the wind measurement from aircraft, of which a few shall be mentioned here. While the carriers are commonly FWA, they cover a wide range, from single-engined light aircraft

(e.g., Crawford and Dobosy, 1992) to twin-engined business jet (e.g., Tjernström and Friehe, 1991) and quad-engined utility aircraft (e.g., Khelif et al., 1999). A similar variety of methodologies is used for the individual proof-of-concept. Widespread are uncertainty propagation of sensor uncertainties (e.g., Tjernström and Friehe, 1991; Crawford and Dobosy, 1992; Garman et al., 2006) and the analysis of specific flight manoeuvres (e.g., Tjernström and Friehe, 1991; Williams and Marcotte, 2000; Kalogiros and Wang, 2002a). Probably due to the higher infrastructural demand, wind tunnel studies (e.g., Garman et al., 2006), comparison to ground based measurements (e.g., Tjernström and Friehe, 1991) and aircraft inter-comparisons (e.g., Khelif et al., 1999) are less common. Often statistical measures are used to express uncertainty, such as repeatability (e.g. $0.03\,\mathrm{m\,s^{-1}}$, Garman et al., 2006), deviation range (e.g. 0.4–$0.6\,\mathrm{m\,s^{-1}}$, Williams and Marcotte, 2000), median differences (e.g. $0.1\pm0.4\,\mathrm{m\,s^{-1}}$, Khelif et al., 1999), or root mean square deviation (e.g. $\geq 0.1\,\mathrm{m\,s^{-1}}$ at $\leq 2\,\mathrm{m\,s^{-1}}$ deviation range, Kalogiros and Wang, 2002a).

The EC technique (e.g., Kaimal and Finnigan, 1994) relies upon the precise measurement of atmospheric fluctuations, including the fluctuations of the vertical wind. Measured from aircraft, the determination of the wind vector requires a sequence of thermodynamic and trigonometric equations (Appendix A). These ultimately define the wind component's frame of reference. Yet, owing to its flexible wing- and aircraft architecture, the dynamics and flow distortion of the WSMA are likely more complex than those of FWA. Therefore the use of well established wind vector algorithms for FWA requires adaptation and correction. Consequently this study first and foremost investigates the feasibility and reliability of the wind measurement from WSMA. Based on these findings the measurement precision will be addressed in a successive study. The WSMA's overall measurement uncertainty was quantified by one standard deviation (σ) for sensor uncertainties provided by the manufacturers (combined effects of temperature dependence, gain error, non-linearity), and one root mean square deviation (RMSD, Appendix B2) for uncertainties from comparison experiments (including the uncertainty of the external reference, where applicable). Due to their analogous role in variance statistics, σ and RMSD are both referred to with one σ for convenience.

After introducing the WSMA and outlining its physical properties, the sensor package for this study is presented. Following the analysis of the aircraft's dynamics, a toolbox is derived for the calibration of the 3-D wind vector measurement and assessment of its uncertainty. It consists of a wind tunnel study, uncertainty propagation and in-flight manoeuvres. The toolbox is used to customize a wind vector algorithm for use with the WSMA. To evaluate this procedure, the final calibration is applied to measurements in the ABL. Wind measurements from the WSMA are compared to simultaneous ground based measurements from sonic detection and ranging (SODAR) and tall tower sonic- and cup anemometer and vane measurements. Based on three independent lines of analysis the overall uncertainty of the WSMA wind measurement is determined.

2 The weight-shift microlight aircraft

According to Joint Aviation Authorities, microlight aircraft are defined as aircraft with a maximum stall speed of 65 km h^{-1} and a take-off mass of no more than 450 kg. Figure 1 shows the weight-shift microlight research aircraft D-MIFU. It consists of two distinct parts, the wing and the trike (the unit hung below the wing, containing pilot, engine and the majority of the scientific equipment). The weight-shift control system is enabled by the pilot's direct application of pitching or rolling moments to the wing via the basebar. Counterbalance is provided by the mass of the trike unit suspended below the wing. Simple procedures for certification of installations on an open aircraft allow a wide spectrum of applications as well as flexible installation of scientific equipment. At an operational airspeed of $\approx$ 100 km h^{-1} D-MIFU can carry a maximum of 80 kg scientific payload from 15 m above ground (a.g.l.) to 4000 m above sea level (a.s.l.). The full performance characteristics can be found in Junkermann (2001).

D-MIFU consists of a KISS 450 cambered wing by Air Creation, France, and the ENDURO-1150 trike manufactured by Ultraleichtflug Schmidtler, Germany. Owing to its aeroelasticity, the tailless delta wing is termed a flex-wing, contributing $\approx$ 15% to the

aircraft weight. The primary parts of the wing structure are the leading edges joined at the nose to the keel tube, which runs the root length of the wing (Fig. 1). Stretched over upper and lower surface is a high strength polyester sail. At a span of 9.8 m and keel length of 2.1 m, the wing provides a surface (S) of 15.1 m^2. It is put under considerable internal loads during rigging, it's form and rigidity being ensured by cross-tubes, rods and a wiring system. The basebar in front of the pilot seat is linked to the keel via two uprights and tensioned flying wires. It provides transmission of pitch and roll forces and is the primary flight control (Gratton, 2001). In the hangpoint on the wing keel the trike is attached to the wing. Since the trike is free to rotate in pitch and roll without hindrance, there is no pendular stability. In this regard the relationship of trike to wing is similar to the relationship of a trailing bomb to its carrier (e.g. HELIPOD, Bange et al., 1999). However trike and wing are fixed in their longitudinal axis, i.e. in the heading direction. The trike does not contribute significantly to the WSMA's lift, but represents a large portion of weight ($\approx$ 85%), drag, and provides all thrust through a 73 kW pusher engine-propeller combination. Flight stability in three axes is based on the offset of torques appearing at different locations on the wing (Cook, 1994). Torques result from wing aerodynamical effects, which sum nearest to neutral (slight nose-down torque for cambered wings) in one point along the wing's chord line, termed the wing's centre of pressure (Fig. 3). The centre of gravity, as far as the wing is concerned, is located in the hangpoint. The net aerodynamical torque is offset by an longitudinal lever arm between the centres of pressure and -gravity, determining the aircraft's trim speed (the airspeed at which the aircraft will fly steadily without pilot input). Moreover increasing airspeed will result in an aeroelastical flattening of the wing, which is in contrast to FWA. This in turn can alter the balance of torsional loads and with it the circulation about the wing (Cook and Spottiswoode, 2006).

2.1 Physical properties

The need to adapt wind calibration procedures designed for fixed-wing aircraft is mainly caused by two structural features of the WSMA. The trike, i.e. the turbulence measurement platform, is mobile for pitching and rolling movements below the wing. Therefore the trike-based flow- and attitude angles must be measured with high resolution, precision and accuracy. Moreover, wing aerodynamics depends on its aeroelasticity with airspeed, and varying flow distortion in front of the wing must be considered. The effects of these WSMA features are not necessarily independent of each other, and may have a different impact on the wind measurement depending on the aircraft dynamics at a particular time. Therefore the WSMA was equipped with motion sensors. On the trike these were placed in the fuselage (Inertial Navigation System, INS) and the wind measuring pressure probe (3-D acceleration), extending ≈ 0.7 m and ≈ 3.5 m forward from fuselage and aft-mounted propeller, respectively (Figs. 1 and 3). Further, the wing was equipped with motion sensors in the hangpoint (3-D acceleration) and atop the wing (3-D attitude). The INS is the most reliable motion sensor (Table 2), since it integrates the complementary characteristics of global positioning system (unbiased) and inertial measurement (precise). Position and velocity are calculated from inertial measurements of 3-D acceleration and 3-D angular rate, and matched with data from two global positioning units using a Kalman filter. The INS outputs 3-D vectors of position, attitude, velocity, angular rates and acceleration.

Airborne wind measurements are susceptible to distortion, since the aircraft itself is (a) a flow barrier and (b) must produce lift to remain airborne (Wyngaard, 1981; Cooper and Rogers, 1991). The aircraft's propeller, fuselage, and wing can be sources of flow distortion. Since the pressure probe is aligned on the longitudinal axis of fuselage and propeller, only little distortion from trike structural features is expected transverse to the pressure probe. Longitudinal and vertical distortions can be expected to carry continuously through the pressure probe location, since the probe is rigidly fixed to the trike. This however is not the case for distortion from the WSMA wing. While the wind measurement encounters lift-induced upwash from the wing (Crawford et al., 1996; Garman et al., 2008), the trike, and with it the pressure probe, has rotational freedom in pitch and roll towards the WSMA wing. In the following we will outline the dependences of upwash generation. The amount of lift (L) generated by the wing

equals the aircraft's sum of vertical forces:

$$L = ma^{\mathrm{g},z}, \tag{1}$$

with the aircraft mass (m) and the vertical acceleration ($a^{\mathrm{g},z}$) in the geodetic coordinate system (GCS, superscript g, positive northward, eastward and downward) at the wing's centre of gravity (measured at, or dislocated to the hangpoint). During level, unaccelerated flight, lift essentially equals the aircraft's weight force, but is opposite in sign. The loading factor (LF) during vertically accelerated flight is then $LF = \frac{L}{mg}$, the ratio of lift- to weight force with $g = 9.81\ \mathrm{m\,s^{-2}}$. Normalizing L for the airstream's dynamic pressure (p_q) and the wing's surface area (S) yields the unit-free lift coefficient (CL):

$$\begin{aligned} CL &= \frac{1}{p_\mathrm{q}} \quad \frac{L}{S} \\ &= \frac{2}{\rho v_\mathrm{tas}^2} \quad \frac{L}{S}, \end{aligned} \tag{2}$$

with wing loading ($\frac{L}{S}$). Moreover p_q in Eq. (2) can be substituted by air density (ρ) and true airspeed (v_tas). In CL the wing's ability to generate lift is determined to be approximately linear with wing pitch. As a consequence of lift generation air rises in front of the wing, which is defined as upwash. Crawford et al. (1996) provide the following parametrization to calculate the upwash velocity (v_up^w) for FWA:

$$\begin{aligned} v_\mathrm{up}^\mathrm{w} &= \frac{1}{\pi^2 n} v_\mathrm{tas} CL \\ &= \frac{1}{\pi^2 n} \frac{v_\mathrm{tas}}{p_\mathrm{q}} \frac{L}{S}, \quad \text{with} \quad \frac{\delta \frac{v_\mathrm{tas}}{p_\mathrm{q}}}{\delta v_\mathrm{tas}} \approx -0.3\ \mathrm{hPa}^{-1}. \end{aligned} \tag{3}$$

Here v_up^w is defined as the tangent on a circle with normalized radius n. Thereby n is the separation distance from the wing's centre of pressure to the position of the pressure probe, normalized by the effective wing chord (Fig. 3). The upwash attack angle ξ is then enclosed by n and the trike body axis X_b. Since the wing is free to rotate in pitch and roll, v_{up}^{w} carries the orientation of the wing coordinate system (WCS, superscript w, positive forward, starboard, and downward). In Eq. (3) v_{up}^{w} varies inversely with n. Furthermore v_{up}^{w} can be expressed either directly proportional to v_{tas} and CL, or directly proportional to relative airspeed ($\frac{v_{tas}}{p_q}$) and $\frac{L}{S}$. Based on these relations a treatment for the wind measurement from WSMA is derived in Sect. 4.1.

2.2 Instrumentation and data processing

Wind measurement by airborne systems is challenging. High resolution sensors are needed to determine the attitude, position, and velocity of the aircraft relative to the earth, as well as the airflow in front of the fuselage. The instrumentation involved in the wind measurement and data acquisition, including the respective manufacturers, is summarized in Table 1. A more detailed description of sensor characteristics and uncertainties is provided in Table 2, while respective locations are displayed in Figs. 1 and 2.

The principle is to resolve the meteorological wind vector from the vector difference of the aircraft's inertial velocity (recorded by the inertial navigation system) and the wind vector relative to the aircraft. To determine the latter, the aircraft was outfitted with a specially designed lightweight five hole half sphere pressure probe (5HP, e.g., Crawford and Dobosy, 1992; Leise and Masters, 1993). The 5HP provides ports of 1.5 mm diameter to directly measure dynamic pressure, static pressure, as well as the vertical and horizontal differential pressures (Fig. 2). To connect these ports to their respective pressure transducers polyetherketone tubings of ≤ 80 mm length and 1 mm inner diameter are used. At a typical true airspeed of 28 m s^{-1} only about 30% and 15% of the dynamic- and differential pressure transducer's range is exploited, respectively. This however enables the 5HP to be used also on faster aircraft such as motorized gliders, e.g. for inter-comparison measurements. Fast temperature was measured by a freely

suspended 50 µm type K thermocouple, while water vapour pressure was measured with a capacitive humidity sensor. Time constants of thermocouple and humidity sensor are < 0.02 s and < 5 s at $v_{tas} = 27$ m s^{-1}, respectively. Humidity readings are used solely to provide the air density correction for the v_{tas} computation. Plug- and-socket connectors with locating pins insure a repeatable location of the 5HP with respect to the INS within $< 0.1°$.

100 Hz temperature and pressure signals pass through hardware (analogue) four-pole Butterworth filters with 20 Hz cut-off frequency to filter high-frequency noise. Filter slope and frequency were chosen to allow miniaturization and comply with the system's 15 Hz bottleneck filter frequency of the infra-red gas analyser for EC flux calculation (not used in this study). The filter leads to a phase shift in the signal of ≈ 20 ms, and the amplitude of a 10 Hz sine signal is reduced by < 1%. The INS data are stored in a standalone system at a rate of 100 s^{-1}. Remaining data streams for the wind computation are stored centrally at a rate of 10 s^{-1} by an in-house developed data acquisition system (embedded Institute for Meteorology and Climate Research data acquisition system, EIDAS). EIDAS is based on a ruggedized industrial computer and a real-time UNIX-like operating system. 5 V analogue signals at ≥ 10 Hz pass through a multiplexer and A/D converter at a resolution of 16 bits. For oversampled variables (100 Hz) the resulting signal is block averaged.

The INS has a latency time for internal calculations of ≈ 4 ms. Yet INS and EIDAS data streams have to be merged to calculate the ambient wind, and later turbulent fluxes. Therefore the resulting time lag between INS and 5HP of ≈ 16 ms has to be considered. The appropriate time shift of one to two 100 Hz increments is determined via lagged correlation. During post-processing the 100 Hz INS data set is then shifted by this increment before block averaging to 10 Hz. A spike test revealed ≈ 7% missing values in the wing attitude data, which were filled via linear interpolation. To enable angular averaging or interpolation, heading angles were transformed from polar to Cartesian coordinates.

3 Wind vector

Approaches to compute the wind vector from fixed-wing aircraft are often similar in principle, though differ considerably in detail (e.g., Tjernström and Friehe, 1991; Williams and Marcotte, 2000; van den Kroonenberg et al., 2008). Therefore, Appendix A details the specific implementation that was found suitable for the wind measurement with our weight-shift microlight aircraft. The system's calibration was arranged bottom-up, i.e. from single instrument to collective application. The procedure starts with the laboratory calibration of the individual sensors, continues with the characterization of flow around the 5HP, and concludes with the treatment of WSMA specific effects on the wind measurement. Finally three independent lines of analysis are used to quantify the overall system uncertainty: (a) uncertainty propagation through respective equations, (b) in-flight testing and (c) comparison of the measured wind vector with ground based measurements.

3.1 Calibration and evaluation layout

Prior to in-flight use, the five hole probe was tested in an open wind tunnel at the Technical University of Munich, Germany, Institute for Fluid Mechanics. Objectives were to (a) confirm the applicability of transformation Eqs. (A5)–(A7) and (b) determine the 5HP's uncertainty in the operational range of the WSMA. The 5HP was mounted on D-MIFU's nose-cap and measuring occurred at airflow velocities ranging from 20 to $32\,\mathrm{m\,s^{-1}}$ (equivalent to 2–6 hPa wind tunnel dynamic pressure). The dynamic pressure at the design stagnation point (i.e. the wind tunnel angles of attack $\tilde{\alpha} = 0^\circ$ and sideslip $\tilde{\beta} = 0^\circ$) was measured at airflow velocity increments of $1\,\mathrm{m\,s^{-1}}$. At increments of $2\,\mathrm{m\,s^{-1}}$ a total of 570 permutations of 10 predefined angles $\tilde{\alpha}$ and $\tilde{\beta}$, each ranging from 0° to +20°, were measured. In addition one-dimensional symmetry tests were performed for six predefined angles $\tilde{\alpha}$ and $\tilde{\beta}$ ranging from −20° to +20° at an airflow velocity of $30\,\mathrm{m\,s^{-1}}$. For the WSMA operational true airspeed of $28\,\mathrm{m\,s^{-1}}$ (or 4.5 hPa dynamic pressure during flight) the uncertainty of the wind tunnel airflow velocity was

0.7% or $\sigma = 0.03$ hPa dynamic pressure. The airflow angles were varied by a calibration robot, the uncertainty in the wind tunnel angles was $\sigma_{\tilde{\alpha},\tilde{\beta}} < 0.1^\circ$ (equal to the alignment repeatability between 5HP and INS). The wind tunnel angles $\tilde{\alpha}$, $\tilde{\beta}$ are flight mechanical angles, defined with respect to the wind tunnel X axis. In contrast the 5HP measured airflow angles α and β are defined with respect to the aerodynamical $\mathrm{X_a}$ axis (Appendix A). In order to allow comparison, the wind tunnel angles must be converted (Boiffier, 1998):

$$\alpha = \tilde{\alpha},$$
$$\beta = \arctan\left(\frac{\tan\tilde{\beta}}{\cos\tilde{\alpha}}\right). \tag{4}$$

The wind vector calculated from airborne measurements is very sensitive to uncertainties in its input variables. Calibration in laboratory and assessment in wind tunnel yield the basic sensor setup. However the effect of sensor and alignment uncertainties on the wind vector is not straightforward, and involves numerous trigonometric functions (Appendix A). To make the influence of individual measured quantities on the wind vector transparent, linear uncertainty propagation models were used (Appendix B1). The intention is to investigate the wind measurement's uncertainty constraint by sensor setup and wind model description under controlled boundary conditions. Because of flow distortion effects (Sect. 2.1) the boundary conditions during flight however are less well known and might be significantly different from the laboratory. Therefore a methodology for in-flight calibration and evaluation was derived. It consists of a WSMA specific calibration model and -flight patterns. These patterns were carried out during three flight campaigns at different sites, each with its characteristic landscape and meteorological forcing:

Lake Starnberg, Germany

The first flight campaign took place from 19 June to 11 July 2008 over Lake Starnberg (47.9° N, 11.3° E). The lake is located in the foreland of the German Alps, that is a slightly rolling landscape (600–800 m a.s.l.) and mainly consists of grassland with patches of forest. The campaign focused on early morning soundings in the free atmosphere above Lake Starnberg.

Lindenberg, Germany

In a second campaign from 14–21 October 2008 comparison flights were carried out at the boundary layer measurement field of the German Meteorological Service, Richard-Aßmann-Observatory, near Lindenberg (52.2° N, 14.1° E). The area lies in the flat North German Plain (40–100 m a.s.l.), where land-use in the vicinity is dominated by an equal amount of agriculture and forests, interspersed by lakes. Flights in the atmospheric boundary layer were conducted under near-neutral stratification (stability parameter $|\frac{z}{L}| \leq 0.2$). However due to the WSMA's low wing loading the wind measurement might be especially susceptible to the influence of thermal turbulence.

Xilinhot, China

To extend the operational range, an additional dataset under conditions approaching free convection ($\frac{z}{L} \ll -0.2$) was included in this study: From 23 June to 4 August 2009 an eddy-covariance flux campaign was performed over the steppe of the Mongolian Plateau. The hilly investigation area south of the provincial capital Xilinhot, Inner Mongolia, China (43.6° N, 116.7° E, 1000–1400 m a.s.l.) is covered by semi-arid grassland, intersected by a dune belt.

A summary of all flights as well as an overview of the synoptic weather conditions is provided in Table 3. In the following, the strategies of the individual flight patterns at these three sites are categorized in five classes and briefly outlined. The first four of

them serve to isolate independent parameters for the flow distortion correction, while the last one is used to compare aircraft to ground based measurements. The patterns are used for the actual calibration and evaluation of the wind measurement in Sect. 4.

Racetrack pattern

The first type of flight pattern consists of two legs parallel to the mean wind direction at constant altitude (one pair), one upstream leg (subscript +) and one downstream leg (subscript −). For any racetrack pair flown at constant true airspeed (v_{tas}), the (assumed homogeneous and stationary) mean wind ($\overline{\boldsymbol{v}^{\mathrm{m}}}$) cancels out (Leise and Masters, 1993; Williams and Marcotte, 2000):

$$\begin{aligned}\overline{|\boldsymbol{v}^{\mathrm{m}}_{\mathrm{gs}}|} &= \frac{1}{2}(\overline{|\boldsymbol{v}^{\mathrm{m}}_{\mathrm{gs},+}|} + \overline{|\boldsymbol{v}^{\mathrm{m}}_{\mathrm{gs},-}|})\\ &= \frac{1}{2}\left((\overline{v_{\mathrm{tas},+}} + \overline{|\boldsymbol{v}^{\mathrm{m}}|}) + (\overline{v_{\mathrm{tas},-}} - \overline{|\boldsymbol{v}^{\mathrm{m}}|})\right)\\ &= \overline{v_{\mathrm{tas}}}.\end{aligned} \tag{5}$$

In this way the INS measured ground speed ($\overline{|\boldsymbol{v}^{\mathrm{m}}_{\mathrm{gs}}|}$) can be used to minimize the difference $|\overline{|\boldsymbol{v}^{\mathrm{m}}_{\mathrm{gs}}|} - \overline{v_{\mathrm{tas}}}|$ by iteratively adjusting dynamic pressure in Eq. (A8). This yields an inverse reference for dynamic pressure, which is solely based on INS data. Since the temperature and static pressure sensitivities of Eq. (A8) are two orders of magnitude lower than that of the dynamic pressure (Table 5), the inverse reference can now be used to adjust the 5HP measured dynamic pressure to in-flight conditions. A total of 14 racetrack pairs at airspeeds ranging from 21 to 32 $\mathrm{m\,s^{-1}}$ were conducted in the calm and steady atmosphere above the ABL (Table 3).

Wind square pattern

The second type of flight pattern consists of four legs flown at constant altitude and constant v_{tas} in the cardinal directions (north (N), east (E), south (S), west (W)). Assuming that the flights were carried out in a homogeneous and stationary wind field, the measured horizontal wind components (v_u^m, v_v^m) should be independent of aircraft heading, i.e. constant at each side of the wind square. With it a potential offset in β can be determined: The offset in β is changed iteratively, until the standard deviation of v_u^m and v_v^m throughout a wind square is minimized. For flights above the ABL, in addition the vertical wind component can be expected to be negligible. A potential offset in α can be determined in a similar fashion to β, however, under the constraint of minimizing the absolute value of the vertical wind component (v_w^m). The wind square pattern further allows to estimate the uncertainties of v_tas and β: Since the flight legs are aligned in the cardinal directions, along-track wind components (v_u^m (N, S), v_v^m (E, W)) are predominantly sensitive to errors in v_tas. Cross-track wind components (v_v^m (N, S), v_u^m (E, W)) are predominantly sensitive to errors in the β. Thus, errors in v_tas and β can be estimated as:

$$\begin{aligned}
\sigma_\mathrm{tas} &= \sqrt{\frac{1}{2}\left(\left(\overline{v_\mathrm{u}^\mathrm{m}}(\mathrm{N}) - \overline{v_\mathrm{u}^\mathrm{m}}(\mathrm{S})\right)^2 + \left(\overline{v_\mathrm{v}^\mathrm{m}}(\mathrm{E}) - \overline{v_\mathrm{v}^\mathrm{m}}(\mathrm{W})\right)^2\right)} \\
\sigma_\beta &= \sqrt{\frac{1}{2}\left(\left(\overline{v_\mathrm{v}^\mathrm{m}}(\mathrm{N}) - \overline{v_\mathrm{v}^\mathrm{m}}(\mathrm{S})\right)^2 + \left(\overline{v_\mathrm{u}^\mathrm{m}}(\mathrm{E}) - \overline{v_\mathrm{u}^\mathrm{m}}(\mathrm{W})\right)^2\right)}. \qquad (6)
\end{aligned}$$

Six wind squares were flown above the ABL at airspeeds from 23 to 29 $\mathrm{m\,s^{-1}}$ (Table 3).

Variance optimization pattern

The third type of flight pattern is a straight and level ABL sounding, intended for EC flux measurement. The assumption made here is that errors in the flow angles increase the wind variance. In contrast to the previous two patterns, this method does not imply homogeneity or stationarity. It can therefore be applied even in the presence of thermal turbulence, i.e. in the convective ABL (Tjernström and Friehe, 1991; Khelif et al., 1999; Kalogiros and Wang, 2002a). Offsets and slopes for α and β were computed to minimize (a) the sum of the wind components variances plus (b) the absolute value

of the mean vertical wind. Here it is expected that, for a sufficiently high number of datasets above approximately level terrain, $\overline{v_w^\mathrm{m}}$ approaches zero. 12 straight and level ABL soundings (or 360 km of flight data, Table 3) at airspeeds from 24 to 28 $\mathrm{m\,s^{-1}}$ between 50 and 160 m above ground were used for this variance optimization.

Vertical wind specific patterns

The fourth type of flight pattern specifically addresses errors in v_w^m, the wind component crucial for EC flux applications. Based on Lenschow (1986) straight-flight calibration patterns were performed above the ABL. These are intended to assess and minimize the possible influence of aircraft (in our case WSMA) trim and dynamics on v_w^m. At airspeeds ranging from 21 to 32 $\mathrm{m\,s^{-1}}$ a total of five vertical wind (VW) specific flights, divided into three sub-patterns, were utilized in this study (Table 3):

VW1 (Level acceleration – deceleration): Whilst the engine's power setting was gradually varied, the wing pitch (and with it lift coefficient) was adjusted to maintain flight altitude. With this pattern the influence of aircraft trim on v_w^m can be determined.

VW2 (Smooth oscillation): Starting from level flight the power setting was slowly varied, while the wing pitch was adjusted to maintain constant v_tas. In consequence, the aircraft ascended and descended about the mean height, while *CL* remained approximately unchanged. VW2 was used to assess the influence of wing pitch and aircraft vertical velocity on v_w^m.

VW3 (Forced oscillation): Starting from level flight the wing pitch was forcibly alternated. The aircraft ascended and descended around the mean height, while power setting remained unchanged. In response aircraft accelerations and velocities, and with it the airflow around the aircraft, changed. VW3 was used to assess the integral influence of vertically accelerated flight on v_w^m, for flights in the ABL e.g. provoked by thermal turbulence.

Comparison to ground based reference measurements

The fifth and last type of flight pattern is a series of comparison measurements between WSMA and ground based measurements. These were carried out at the boundary layer measurement field of the German Meteorological Service, Richard-Aßmann-Observatory, near Lindenberg. The lower part of the ABL was probed by a 99-m tower and a SODAR with their base at 73 m a.s.l. The 99-m tower provided cup measurements (10 min averages) of wind speed at four levels (40, 60, 80, and 98 m a.g.l.), the wind direction was measured with vanes at heights of 40 and 98 m a.g.l. (10 min averages). Sonic anemometers mounted at the tower provided turbulent wind vector measurements at 50 and 90 m a.g.l. The SODAR wind vector profiles (15 min averages) reached, at increments of 20 m, from 40 to 240 m a.g.l. In addition a reference for static pressure was provided at 1 m a.g.l. 17 cross-shaped patterns (van den Kroonenberg et al., 2008), with flight legs of 3 km centred between tower and SODAR, were performed at 24 and 27 $\mathrm{m\,s^{-1}}$ airspeed (Table 3). The flights were carried out at the approximate sounding levels of tower and SODAR (50, 100, 150, 200 and 250 m a.g.l.). This allows a direct comparison of WSMA and ground based measured wind components. Aircraft and sonic wind measurements were filtered using the stationarity test for wind measurements by Foken and Wichura (1996). SODAR, cup and vane data were stratified for the best quality rating assigned by the German Meteorological Service. Simultaneous wind data of WSMA and ground based measurements were accepted for comparison only if they agreed to within ±20 m height above ground (which equals $\approx 2\sigma$ of variations in WSMA altitude). This data screening resulted in a total of 20 data couples (between WSMA and cups/vanes, sonics and SODAR) for $v_{\mathrm{uv}}^{\mathrm{m}}$, and 19 data couples for $v_{\mathrm{w}}^{\mathrm{m}}$. Compared to cups/vanes, sonics and SODAR, the WSMA soundings were on average higher above ground by 0.1 ± 5.5, 8.7 ± 5.6, and 0.5 ± 5.3 m, respectively.

4 Application to weight-shift microlight aircraft

To understand operational requirements for setup and calibration of the wind vector measurement, aircraft attitude and dynamics were assessed for a straight and level boundary layer flight (Table 3, variance optimization flight on 31 July 2009). Variations in true airspeed and aircraft vertical movement (Fig. 4) were mainly resulting from thermal turbulence (labile stratification, stability parameter $\frac{z}{L} \approx -0.9$). Attitude angles (Θ^{b}, Φ^{b}) indicate constant upward pitching and anti-clockwise roll of the trike, respectively. Pitching as well as rolling increase in magnitude with v_{tas}, i.e. power setting of the engine. The pitching moment can be understood as a result of imbalanced increase of aerodynamic resistance of wing (high) and trike (low) with v_{tas}. This is confirmed by an estimate of the attack angle (α), which shows fewer variation due to alignment with the streamlines, though alike Θ^{b} increases with v_{tas} ($\approx 0.4^{\circ}$ per $\mathrm{m\,s^{-1}}$). The rolling moment can be understood as counter-balance of the clockwise rotating propeller torque. In addition side-slipping of the trike over its port side was detected from an estimate of the sideslip angle (β), increasing at a rate of $\approx -0.6^{\circ}$ per $\mathrm{m\,s^{-1}}$ with v_{tas}. The operational range in α and β estimates were found $\approx |15^{\circ}|$, averaging to $6.0 \pm 1.8^{\circ}$ and $-5.5 \pm 3.2^{\circ}$, respectively (Fig. 4). Following the lift Eq. (2), wing pitch decreases with v_{tas}. That is, with increasing v_{tas} the noses of wing and trike approach each other. Wing roll does not display dependence on v_{tas}, i.e. no counter reaction on propeller torque or trike roll. The wing loading factor (*LF*) was found to vary within a range of $\sigma \approx 0.1$ g (Fig. 4), from which the upwash variation in front of the wing can be assessed.

Using five hole probe measured v_{tas} in Eq. (3) the upwash velocity ($v_{\mathrm{up}}^{\mathrm{w}}$) at 5HP location was determined to $1.52 \pm 0.19\,\mathrm{m\,s^{-1}}$. D-MIFU is travelling at low airspeed and has a small relative separation (n) between wing and 5HP. Both factors lead to an increase in $v_{\mathrm{up}}^{\mathrm{w}}$. Various research aircraft have been assessed with regard to upwash generation (Crawford et al., 1996), compared to which D-MIFU ranges mid-table. This can be ascribed to the low wing loading, which is a fraction of those of fixed-wing aircraft, and decreases $v_{\mathrm{up}}^{\mathrm{w}}$. Wing loading, and with it $v_{\mathrm{up}}^{\mathrm{w}}$, are directly proportional to vertical acceleration and aircraft mass in Eq. (1). Hence $\sigma \approx 10\%$ variation in LF (Fig. 4) accounts for most of the variance in $v_{\mathrm{up}}^{\mathrm{w}}$. In addition aircraft mass can vary during the flight due to fuel consumption (±4%) and among measurements due to weight differences of pilots (±2%). Due to the trike's rotational freedom, upwash about the wing's centre of pressure can partially translate into along- and sidewash (longitudinal and transverse to the trike body, respectively) at the 5HP location in the trike body coordinate system (BCS). Mean aerodynamic chord theory yields the centre of pressure's position of the wing within 0.2 m or < 10% chord length of the centre of gravity. Assuming the centres of pressure and gravity to coincide, the pitch difference between wing and trike can be neglected, and $v_{\mathrm{up}}^{\mathrm{w}}$ is easily transformed into the BCS: The transformation Eq. (A13) was carried out about zero heading difference, the upwash attack angle ($\xi = -41.9 \pm 0.3^\circ$), and the roll difference between wing and trike. Wing upwash net effect at the 5HP location was then directed forward, right and upward with $1.01 \pm 0.13\,\mathrm{m\,s^{-1}}$, $0.12 \pm 0.13\,\mathrm{m\,s^{-1}}$, and $-1.12 \pm 0.14\,\mathrm{m\,s^{-1}}$ in trike body coordinates (Fig. 5).

4.1 Wind measurement calibration

The sensitivity of the wind model description was analysed by linear uncertainty propagation models (Appendix B1). The first model in Eq. (B1) permits to express the sensitivity of the wind computation as a function of attitude angles, flow angles and true airspeed. It was carried out for two reference flight states at $v_{\mathrm{tas}} = 27\,\mathrm{m\,s^{-1}}$. In State 1 attitude and flow angles were assumed small (1°), as it would be typical for calm atmospheric conditions. In State 2 attitude (10°) and flow angles (−15°) were approximately increased to their 95% confidence interval extremes during soundings in the convective ABL (Fig. 4). Uncertainties of 1° and $0.5\,\mathrm{m\,s^{-1}}$ were assumed for angular- and v_{tas} measurements, respectively. From State 1 it can be seen that the major uncertainty in the horizontal wind components ($v_{\mathrm{uv}}^{\mathrm{m}}$) originates from v_{tas}, sideslip angle (β) and heading angle (Ψ), where β and Ψ carry similar sign and sensitivity (Table 6). On the contrary, the vertical wind component ($v_{\mathrm{w}}^{\mathrm{m}}$) is similarly sensitive to

attack angle (α) and pitch angle (Θ), yet with reversed sign. As compared to State 1, in State 2 the absolute uncertainties in the horizontal ($|\Delta v_{\mathrm{uv}}^{\mathrm{m}}|$) and vertical ($|\Delta v_{\mathrm{w}}^{\mathrm{m}}|$) wind components are increased by 24% and 18%, respectively. The increase however does not originate from the most sensitive-, but from formerly negligible terms such as trike roll (Φ^{b}). The latter now account for up to 50% of $|\Delta v_{\mathrm{uv}}^{\mathrm{m}}|$ and 37% of $|\Delta v_{\mathrm{w}}^{\mathrm{m}}|$. Similar sensitivity analyses were carried out for α in Eq. (A5), β in Eq. (A6) and the thermodynamic derivation of v_{tas} in Eq. (A8). Also here $v_{\mathrm{tas}} = 27\,\mathrm{m\,s^{-1}}$ was assumed as reference state, parametrized as 3.7 hPa dynamic pressure (p_{q}), 21 °C static temperature, 850 hPa static pressure, and 9.5 hPa water vapour pressure. Derived sensitivities indicate a dominant dependence of α and β on their respective differential pressure measurement, as well as on p_{q} (Table 5). In case of v_{tas} sensitivity on the p_{q} measurement clearly prevails. This procedure allows to separate, and consequently further concentrate on, the variables most sensitive to the wind vector calculation. For $v_{\mathrm{w}}^{\mathrm{m}}$, the central wind component in the eddy-covariance flux technique, the variables to focus calibration effort on are α, Θ and p_{q}. Likewise correct readings of β, p_{q} and Ψ are of greatest importance for the calculation of $v_{\mathrm{uv}}^{\mathrm{m}}$.

Due to the same adiabatic heating effect (ram rise) as in Eq. (A9), the temperature measured by the thermocouple might be slightly higher than the static temperature intrinsic to the air. At the same time the measured temperature is smaller than the total temperature at the stagnation point on the tip of the 5HP, since the air at the thermocouple is not brought to rest. Even at peak $v_{\mathrm{tas}} = 30\,\mathrm{m\,s^{-1}}$ of the WSMA the ram rise of 0.4 K does not surpass the overall uncertainty of the thermocouple (Table 2). As a practical advantage of the slow flying WSMA therefore no fractional "recovery factor" correction as known from faster fixed-wing aircraft needs to be introduced (Trenkle and Reinhardt, 1973). Using above sensitivity analysis the associated uncertainty amounts to $0.02\,\mathrm{m\,s^{-1}}$ in v_{tas}. According to the parametrizations (5) and (7) in Foken (1979) the error caused by solar radiation intermittently incident at the unshielded thermocouple was estimated to be < 0.05 K. Since no radiation shielding was applied, both temperature errors were included in the uncertainty propagation (Table 5).

The actual calibration sequence was organized in seven steps. To reduce scatter and computation time, 10 Hz aircraft data were block averaged to 1 Hz for steps D–G:

Step A – Laboratory: Initial calibration of all A/D devices.

Step B – Wind tunnel: Assessment of attack- (α) and sideslip angle (β) and first correction of dynamic pressure (p_q).

Step C – Tower fly-bys: Adjustment of static pressure (p_s).

Step D – Racetracks: Second p_q correction.

Step E – Wind squares: First estimate of α and β correction.

Step F – Variance optimization: Second estimate of α and β correction.

Step G – Vertical wind treatment: Relation of measured upwash to lift coefficient, iterative optimization with step E–F.

Step A – Laboratory

Calibration coefficients from laboratory and all successive steps are summarized in Table 4. Residuals are propagated together with sensor uncertainties as provided by the manufacturers. The resulting uncertainties are summarized in Table 5.

Step B – Wind tunnel

Since the wind tunnel was too small for the complete aircraft, the setup was reduced to the five hole probe and the aircraft's nose-cap. Therefore the actual flow distortion during flight was not included in this step. For angles of attack (α) and sideslip (β) within $\pm 17.5^\circ$ the first-order approximations Eqs. (A5)–(A6) were most effective for deriving flow angles from our miniaturized 5HP. Root mean square deviation (RMSD) and bias (BIAS) amounted to 0.441, 0.144° and 0.428, 0.047° for α and β, respectively,

with a Pearson Coefficient of determination $R^2 > 0.99$. Residuals did not scale with true airspeed, but resulted from incomplete removal of α and β cross dependence (Fig. 6). Yet the probe design was working less reliably with the exact solutions for flow angle determination (e.g. Eq. (7) in Crawford and Dobosy, 1992). On the other hand use of a calibration polynomial as suggested by Bohn and Simon (1975) has the advantage that it does not assume rotational symmetry. A fit of the calibration polynomial yielded high precision, however did not prove robust for in-flight use and was discarded. For dynamic pressure ($p_{q,A}$, subscript upper-case letters A–G indicating calibration stage), offset (0.22 hPa) and slope (1.05) were corrected from zero working angle measurements. Applying the pressure drop correction Eq. (A7) thereafter reduced the scatter significantly, in particular for elevated working angles (Fig. 6). Below 20° working angle ($\approx 15^\circ$ flow angle) $p_{q,B}$ was slightly overestimated, above this a loss of only ≈ -0.1 hPa remained. RMSD and BIAS amounted to 0.042 and 0.012 hPa, respectively, with $R^2 = 0.999$.

Step C – Tower fly-bys

A wing induces lift by generating lower pressure atop and higher pressure below the airfoil. Since the five hole probe is measuring at a position being located below the wing, the static pressure (p_s) measurement is potentially biased. Though sensitivity of the wind computation on p_s is low (Table 5), correct air densities are required for EC computations. An offset adjustment was estimated to -2.26 ± 0.43 hPa from comparison with tower based measurements (Table 3). No dependence of the adjustment on true airspeed or lift coefficient could be detected. This can most probably be attributed to the small v_{tas} range of the WSMA.

Step D – Racetracks

For racetrack and wind square flights, inhomogeneous flight legs were discarded using the stationarity test for wind measurements by Foken and Wichura (1996). Respective optimality criteria Eqs. (5)–(6) were applied to 1 Hz block averages of the remaining legs. The dynamic pressure inverse reference from racetracks suggests an offset (0.213 hPa) and slope (1.085) correction. Without considering additional dependences, the fit for different power settings is well determined with 0.115 hPa residual standard deviation and $R^2 = 0.974$. We have seen that the upwash ($v_{\mathrm{up}}^{\mathrm{w}}$) in front of the wing of the WSMA is effective forward, right and upward at the 5HP location in body coordinate system (Fig. 5). That is, the magnitude of dynamic pressure ($p_{\mathrm{q,B}}$) measured at the 5HP tip, and with it the calculated true airspeed, is reduced by $v_{\mathrm{up}}^{\mathrm{w}}$. Therefore the slope correction from racetracks was used to account for the loss in $p_{\mathrm{q,B}}$ magnitude due to upwash in front of the wing. The suggested offset was considered as inversion residue of atmospheric inhomogeneities during the racetrack manoeuvres, and consequently discarded.

Step E – Wind squares

Over all wind square flights the optimality criteria for horizontal and vertical wind components were averaged. Offsets for α (0.005 rad) and β (−0.012 rad) were iteratively adjusted to minimize this single measure (Table 3).

Step F – Variance optimization

From the variance optimization method a second set of offsets for α (0.017 ± 0.003 rad) and β (-0.014 ± 0.001 rad) was found. The optimality criteria were applied to each leg individually and the offsets determined were averaged. The estimates differ from those for the wind squares by 0.6° for α and by 0.1° for β. While the deviation for β lies within the installation repeatability, the deviation for α corresponds to $\approx 0.3\,\mathrm{m\,s^{-1}}$ uncertainty in the vertical wind (Table 6). The wing's upwash in Eq. (3), and its variation due to different aircraft trim was considered as one possible reason for this deviation: While flying level with similar power setting, flights in denser air in the atmospheric boundary layer (e.g. variance optimization flights) require a smaller lift coefficient, i.e. less wing

pitch, than flights in the less dense air in the free atmosphere (e.g. wind square flights). That is *CL* in Eq. (2) is inversely proportional to air density. For flights in the ABL, in particular thermal turbulence is likely to additionally alter the wing loading, and with it *CL* in Eq. (2).

Step G – Vertical wind treatment

Among all the wind components the vertical wind measurement is of prevailing importance to reliably compute eddy-covariance fluxes. Correspondingly its assessment and treatment is the centrepiece of this calibration procedure. To disentangle the comprehensive sequence of assessment and treatment, Step G is further divided into five sub-steps:

Step G1 – Net effect of aircraft trim and wing loading.

Step G2 – Reformulation of the upwash correction.

Step G3 – Parametrization of aircraft trim and wing loading effects.

Step G4 – Parametrization of offsets.

Step G5 – Iterative treatment of cross dependences.

Step G1 – Net effect of aircraft trim and wing loading

The net effect of changing aircraft trim and wing loading was investigated with the forced oscillation (VW3) flight pattern. During the flight on 25 June 2008 the wing pitching angle was modified by ±5° and the maximum vertical velocity reached $|4|\,\mathrm{m\,s^{-1}}$ (Fig. 7). It is evident that the modelled upwash ($v_{\mathrm{up}}^{\mathrm{w}}$) is linearly dependent on the lift coefficient, as defined in Eq. (3). The actual variations in measured vertical wind ($v_{\mathrm{w}}^{\mathrm{m}}$) however were smaller by one order of magnitude and phase inverted compared to the modelled upwash or *CL*. Assuming a constant vertical wind, not necessarily but likely approaching zero above the ABL, measured variations in v_w^m are referred to as "measured upwash". As opposed to the parametrization by Crawford et al. (1996) for fixed-wing aircraft, measured upwash at the five hole probe location is highest during fast flight at low *CL*. Yet, also in contrast to FWA, the WSMA's wing-tip and trike nose approach each other with increasing airspeed (Sect. 4). The wing's centre of pressure is within $< 10\%$ chord length of the centre of gravity. Considering this distance, wing pitching by -5° would result in a decrease of the normalized distance between centre of pressure and 5HP (n), by $\approx -1\%$. Though modelled upwash inversely varies with n in Eq. (3), the approach of wing and trike alone can not explain the upwash phase inversion. On the other hand, the wing flattens aeroelastically with true airspeed. That is, with increasing v_tas the wing's cambering and with it the relative lift generation is attenuated. Therefore the wing upwash of a WSMA can neither be parametrized nor corrected with the Crawford et al. (1996) model alone. Garman et al. (2008) on the other hand proposed to correct for upwash by considering the actual wing loading factor (*LF*), which carries information on the aircraft's vertical acceleration. In contrast to the study of Garman et al. (2008), WSMA weight, fuel level as well as dynamic pressure (p_q) are known. Therefore *CL* can be directly determined in Eq. (3) and used instead of *LF*. This has the advantage that additional information on the aircraft's trim is included: As formulated in Eq. (2), p_q carries information on v_tas at given air density. Over eight independent flights of patterns VW1, VW2 and VW3 measured upwash correlated with *CL* (-0.53 ± 0.16), change in v_tas (0.57 ± 0.16), and wing pitch (-0.50 ± 0.20).

Step G2 – Reformulation of the upwash correction

Crawford et al. (1996); Kalogiros and Wang (2002b) have shown that the upwash Eq. (3) can be reformulated as a function of *CL* in the 5HP measured attack angle (α). Yet, as opposed to FWA, the WSMA is defined in two different coordinate systems, those of the wing (upwash) and the trike (5HP measurement, Fig. 3). Therefore an

upwash correction in α would not explicitly consider the mobility of the trike in the wing circulation. As shown above only minor uncertainty would be introduced for pitching movements, though rolling movements and their possible influence would be left out. Consequently wind measurements during horizontal manoeuvres would not be covered, which however are not the subject of this study. In return correcting the upwash in α yields several advantages compared to explicitly modelling and subsequently subtracting the upwash: one explanatory variable is sufficient to explain the upwash variability effectively incident at the 5HP. With it a potential phase shift between variables measured in the wing and the trike body coordinate systems, as well as additional coordinate transformations are omitted. Therefore the upwash variability was treated for straight and level flight (such as during EC soundings) using a linear model in α:

$$\begin{aligned}\alpha_\infty &= \alpha_\mathrm{A} - \alpha_\mathrm{upw} \\ &= \alpha_\mathrm{A} - \left(\alpha_\mathrm{upw,off} + \alpha_\mathrm{upw,slo} CL\right),\end{aligned} \tag{7}$$

with α_∞ the (desired) free air stream angle of attack, α_A being the 5HP derived attack angle, and α_upw an additive attack angle provoked by the upwash with $\alpha_\mathrm{upw,off}$ and $\alpha_\mathrm{upw,slo}$ being its constant part and sensitivity on *CL*, respectively.

Step G3 – Parametrization of aircraft trim and wing loading effects

For vertical wind specific flights (VW) above the ABL, α in Eq. (A11) was changed iteratively until yielding a vertical wind (v_w^m) of zero. Subtracting this inverse reference of α_∞ from α_A gives us an estimate of α_upw. To reduce scatter, α_upw was averaged after binning over increments of 0.01 *CL*. From this binned and averaged data $\alpha_\mathrm{upw,off}$ and $\alpha_\mathrm{upw,slo}$ were obtained with a linear fit (Fig. 8). Scatter for the level acceleration-deceleration (VW1) flight and the forced oscillation (VW3) flight (both on 25 June 2008) is significantly reduced by implementing the binning procedure. Before binning, the VW1 flight shows a slight hysteresis, probably due to the accelerating- and decelerating legs. Non-binned values of the VW3 flight are considerably more scattered than for VW1. This can be attributed to the rising and sinking process of the aircraft and changing flow regimes about the wing during load change at the turning points. Fitted coefficients differed slightly between the two flights. The analysis was continued with the coefficients of the better determined VW1 flight ($R^2 = 0.85$), which amount to $\alpha_{\text{up,off}} = 0.031$ rad and $\alpha_{\text{upw,slo}} = -0.027$ rad. That is α_{A} would be overestimated by $\approx 1.7°$ if the WSMA could fly at zero lift. The effect decreases with slower flight at a rate of $\approx -1.7°$ per CL. The correction reduces the vertical wind fluctuations for systematic deviations resulting from varying wing trim (53%, relative to the bias-adjusted overall fluctuation) and wing loading (16%) for above named VW1 and VW3 flights, respectively. For the VW3 flight (Fig. 7) the decorrelation of v_{w}^{m} with v_{tas} improves from 0.79 to −0.11, and the decorrelation with wing pitch improves from −0.78 to 0.17. Assuming zero vertical wind, RMSD and BIAS slightly improved from 0.17 and 0.15 m s^{-1} to 0.13 and −0.11 m s^{-1}, respectively. Lenschow (1986) proposed a 10% criteria for the effect of the aircraft's vertical velocity ($v_{\text{gs}}^{\text{m},z}$) on v_{w}^{m}. It is employed as an operational limit by the Research Aviation Facility of the US National Centre for Atmospheric Research (NCAR, Tjernström and Friehe, 1991). Using the upwash correction this measure was improved from 3.8% to 2.7% (σ). A slight trend in v_{w}^{m} remains. The correction was also applied to two smooth oscillation (VW2) patterns. The flight on 24 June 2008 was conducted in less calm air and two different power settings were applied (Fig. 9). The correction changed overall RMSD and BIAS from 0.26 and 0.13 m s^{-1} to 0.25 and −0.13 m s^{-1}, respectively. That is the quality measures did not indicate significant improvement, but the vertical wind BIAS was inverted. However after correction the change in power settings (4800–5000 s slow, 5200–5400 s fast) did not alter the offset in v_{w}^{m} anymore (correlation of v_{w}^{m} with v_{tas} decreased from 0.42 to 0.21). The dependence on vertical movement decreased only slightly from 14.7% to 13.5% (σ), however correlation of v_{w}^{m} with $v_{\text{gs}}^{\text{m},z}$ is < 0.02. Due to the less calm atmosphere σ might not be representative for their cross dependence in this case. The VW2 flight on 25 June 2008 was again conducted in

calm air (Fig. 9). Here our correction leads to a change in RMSD and BIAS from 0.22 and 0.20 m s^{-1} to 0.09 and −0.02 m s^{-1}. After correction the dependence on vertical aircraft movement increased slightly from 7.7% to 8.3% (σ), which still well agrees with the limit used by NCAR.

Step G4 – Parametrization of offsets

We learned from the VW3 pattern (Fig. 7), that calculation of v_{w}^{m} was improved for flights which include vertical accelerations. This is an important step, since due to its low wing loading the WSMA is more susceptible to e.g. convective gusts in the ABL than large FWA's. These gusts also transport the scalars to be investigated, i.e. vertical wind and scalar quantity are correlated in the gust. Not accounting for the negative correlation of measured v_{w}^{m} with CL would decrease the magnitude of fluctuations in v_{w}^{m}, such spuriously decreasing fluxes derived from the airborne measurements. From the VW2 pattern we have seen that the decorrelation of v_{w}^{m} with v_{tas} was improved (Fig. 9). Also v_{w}^{m} was proven independent of slow aircraft rising and sinking manoeuvres, such as they are occurring in the ABL while following topographic features at constant altitude above ground. After applying the correction, BIAS in v_{w}^{m} was negative, ranging from −0.13 to −0.02 m s^{-1}. Assuming independence of v_{w}^{m} from v_{tas}, the detected BIAS depends on $\alpha_{\text{up,off}}$ in Eq. (7). Both, $\alpha_{\text{up,off}}$ and $\alpha_{\text{upw,slo}}$ were determined using the VW1 flight on 25 June 2008 during ambiguous cyclonality atop and below measurement altitude (Table 3). In Fig. 8 the determination of $\alpha_{\text{upw,slo}}$ depends on the change of CL, while the offset $\alpha_{\text{up,off}}$ depends on the ambient vertical wind. During the inverse reference procedure v_{w}^{m} was forced to zero while, e.g. in an anticyclone, subsidence occurs. In such a situation $\alpha_{\text{up,off}}$ would be underestimated. During the VW flights on 24 and 25 June 2008, cyclonality and BIAS in v_{w}^{m} both changed. While $\alpha_{\text{upw,slo}}$ is insensitive, no constant $\alpha_{\text{up,off}}$ could be determined from the VW flights. At this point the variance optimization flights in the ABL are of importance.

Assuming constant ABL height (approximately fulfilled for noontime EC soundings) the second optimality criteria states that due to mass conservation $\overline{v_w^{\mathrm{m}}}$ approaches zero for a sufficiently high number of datasets. With it $\alpha_{\mathrm{up,off}}$ was determined directly from ABL flights. Using the first variance optimization optimality criteria, i.e. the minimization of the wind variance, also α and β slopes were tested.

Step G5 – Iterative treatment of cross dependences

An approach similar to Eq. (7), the explanation of upwash in α, was used to explain sidewash in β:

$$\beta_\infty = \beta_{\mathrm{A}} - \left(\beta_{\mathrm{upw,off}} + \beta_{\mathrm{upw,slo}} CL\right), \tag{8}$$

using the calibration criteria of the wind square flights for parametrization. Compared to the upwash parametrization, sidewash was found to be modest ($\beta_{\mathrm{upw,off}} = -0.004$ rad) and less sensitive regarding CL ($\beta_{\mathrm{upw,slo}} = -0.010$ rad, Table 4). This is in line with the first attempt to resolve the circulation around a FWA wing and trike movement independently (Fig. 5). Using Eq. (A11) cross dependence occurs between the parametrizations in α and β. This problem was solved by iterating the optimality criteria for wind square, vertical wind, and variance optimization flights in sequence. The order of this sequence, i.e. first optimizing for the horizontal wind components ($v_{\mathrm{uv}}^{\mathrm{m}}$), then for the vertical wind component ($v_{\mathrm{w}}^{\mathrm{m}}$), was chosen due to their different order of magnitude and importance for EC application. Spurious contamination with $v_{\mathrm{w}}^{\mathrm{m}}$ would change $v_{\mathrm{uv}}^{\mathrm{m}}$ only by a tiny fraction. The other way around however would result in considerably higher contamination in $v_{\mathrm{w}}^{\mathrm{m}}$. The final calibration coefficients are summarized in Table 4.

4.2 Wind measurement evaluation

After completing all calibration steps, the wind measurement with the WSMA was evaluated. The evaluation was carried out in three lines of analysis, (a) uncertainty

propagation, (b) wind square flights, and (c) comparison to ground based wind measurements. For a true airspeed of 27 m s^{-1} the propagation of uncertainties in sensors (flow angle differential pressures, dynamic- and static pressures, static temperature, and water vapour pressure), their basic calibration and wind model description yield an uncertainty (σ) of 0.76°, 0.76°, and 0.34 m s^{-1} in attack angle (α), sideslip angle (β) and true airspeed, respectively (Table 5). Feeding the input uncertainty Eq. (B1) with these quantities extends the uncertainty propagation to the wind components (Table 6). The input error is formulated worst case, and parametrized at the extremes of the attitude and flow angle 95% confidence intervals. In addition the uncertainty of the inertial navigation system (0.02 m s^{-1}) was considered in the wind vector Eq. (A1). This allows to estimate the maximum potential uncertainty by sensor setup and wind model description. The results for the maximum overall uncertainty bounds are 0.66 and 0.57 m s^{-1} for the horizontal ($v_{\mathrm{uv}}^{\mathrm{m}}$) and vertical ($v_{\mathrm{w}}^{\mathrm{m}}$) wind components, respectively.

Figure 10 shows the results of all wind square flights. For wind velocities > 2 m s^{-1} $v_{\mathrm{uv}}^{\mathrm{m}}$ determined for individual legs deviate less than 10% from the average for the entire square. The residuals did not scale with the average wind velocity, to a greater degree they are likely to result from an incomplete removal of wind field inhomogeneities over the 12 km long flight paths. Therefore a horizontal wind velocity of 2 m s^{-1} can not be considered as a detection limit for wind measurements from WSMA. Also no systematic deviation for aircraft orientation could be detected. However $v_{\mathrm{w}}^{\mathrm{m}}$ shows a slight sensitivity of -0.05 on v_{tas} ($R^2 = 0.46$). Using the cardinal direction evaluation criteria Eq. (6), RMSD in α_∞, β_∞ and $|\boldsymbol{v}_{\mathrm{tas}}^{\mathrm{m}}|$ were computed to 0.31, 0.33 and 0.26 m s^{-1}, respectively. These compare well to the results from the uncertainty propagation (Tables 5 and 6), which amount to 0.31, 0.36 and 0.34 m s^{-1} for α_{A}, β_{A} and v_{tas}, respectively.

Figure 11 shows a qualitative comparison of WSMA and ground based wind measurements for the flight on 15 October 2008. The vertical profile shows an equal number of flights at 24 and 27 m s^{-1} true airspeed. Despite one outlier in $v_{\mathrm{v}}^{\mathrm{m}}$ and $v_{\mathrm{w}}^{\mathrm{m}}$ at 120 m a.g.l., no distinct differences in average wind velocities between ground based measurements and WSMA are apparent. The comparability of WSMA and ground based wind measurement was further quantified by calculating RMSD and BIAS for all measurements accepted for the comparison (Table 3). The impact of calibration steps C–G on these measures is displayed in Fig. 12. The measurement of the horizontal wind components ($v_{\mathrm{uv}}^{\mathrm{m}}$) was mainly improved (14%, relative to the initial uncertainty) by means of the in-flight dynamic pressure correction (step D). After the wind square analysis (step E) the measurement was not further improved nor deteriorated. Yet the vertical wind measurement ($v_{\mathrm{uv}}^{\mathrm{m}}$) receives its greatest improvement (31%) during steps F–G, i.e. variance optimization and vertical wind specific patterns: During these steps BIAS and dBIAS, i.e. its dependence on v_{tas}, were reduced. In contrast to the findings from the wind square analysis, with a sensitivity of $\approx +0.05$ a slight positive dependence of all wind components on v_{tas} remained. Considering all data couples between WSMA and ground based measurements, RMSD and BIAS amount to 0.50 and $-0.07\,\mathrm{m\,s^{-1}}$ for $v_{\mathrm{uv}}^{\mathrm{m}}$ and 0.37 and $-0.10\,\mathrm{m\,s^{-1}}$ for $v_{\mathrm{w}}^{\mathrm{m}}$, respectively. In addition to the above mentioned outlier, two more suspects were identified for the flight on 18 October 2008, again concurrent for $v_{\mathrm{v}}^{\mathrm{m}}$ and $v_{\mathrm{w}}^{\mathrm{m}}$. A possible explanation is the increased land surface heterogeneity sensed by the aircraft while travelling through the wind field. On the northern and western limbs of the aircraft cross pattern, forest patches of $\geq 200\,\mathrm{m}$ edge length interrupt the flat arable land immediately upwind. Therefore WSMA measurements can include turbulence and wake effects generated at the forest edges. In contrast tower measurements are not subject to comparable roughness changes until $\approx 2\,\mathrm{km}$ in upwind direction. Omitting the three outliers from the statistics, RMSD and BIAS between WSMA and ground based measurements improve to 0.39 and $-0.11\,\mathrm{m\,s^{-1}}$ for $v_{\mathrm{uv}}^{\mathrm{m}}$ and 0.27 and $-0.10\,\mathrm{m\,s^{-1}}$ for $v_{\mathrm{w}}^{\mathrm{m}}$, respectively.

4.3 Discussion

Distortions of the wind measurement originating from the aeroelastic wing and trike structural features were successfully handled for straight, vertically accelerated flight.

Yet the treatments integral to Eqs. (A7), (7) and (8) still leave room for improvement: Compared to ground based measurements the aircraft underestimated the wind components $\approx -0.1\,\mathrm{m\,s^{-1}}$. A possible reason could be the discarded offset during the dynamic pressure (p_{q}) in-flight calibration (Sect. 4.1). Rather forcing the linear fit to zero would slightly enhance the slope of p_{q} and with it compliance to the aircraft's inertial speed.

During the wind square and comparison flights contradictory sensitivities (regression slope -0.05 versus $+0.05$) of the wind components on the true airspeed were found. For the variability in v_{tas} during a thermally turbulent flight in the atmospheric boundary layer ($\sigma = 1.24\,\mathrm{m\,s^{-1}}$, Fig. 4) this corresponds to $\pm 0.06\,\mathrm{m\,s^{-1}}$ deviation in the wind components. Since this deviation is one order of magnitude lower than the system's input uncertainty, it was not further treated.

The lift coefficient is used as sole explanatory variable in the linear calibration models Eqs. (7) and (8). This treats the influence of aircraft trim (i.e. dynamic pressure) and vertical acceleration (i.e. loading factor) on the wind measurement with similar sensitivity. The study by Visbal and Shang (1989) however shows that the flow field response of airfoils to pitch oscillations depends on the excitation frequency. This indicates that an independent upwash correction is desirable for steady state and dynamic flight modes. Such procedure would however require infinitely more in-flight data and analytical effort in order to isolate independent parameters. In return it could address forenamed dependence of the wind components on v_{tas} and additionally allow for superior wind measurements during horizontal manoeuvres.

5 Conclusions

We have shown that carefully computed wind vector measurements using a weight-shift microlight aircraft are not inferior to those from other airborne platforms. A 10% limit of contamination of the wind components by the aircraft movement, as used by the US National Centre for Atmospheric Research, was fulfilled even during severe vertical manoeuvring. For straight, vertically accelerated flights as during eddy-covariance applications, three independent lines of analysis yield comparable uncertainty. This convergence is remarkable and emphasizes the integrity of sensing elements and wind model description. The procedure further enables to quantify the overall operational uncertainty (root mean square deviation) to $0.4\,\mathrm{m\,s^{-1}}$ for the horizontal and $0.3\,\mathrm{m\,s^{-1}}$ for the vertical wind components.

Independent consideration of trike movement and wing circulation according to the fixed-wing aircraft theory was not successful. Instead flow distortion of fuselage, propeller and wing were minimized by an approach integrated in the dynamic pressure and flow angle computations. The magnitude of distortion was treated as slope correction in the dynamic pressure computation. The distortion's distribution in components longitudinal, transverse and vertical to the wind measurement was subsequently parametrized in the attack- and sideslip angle computations. The lift coefficient was successfully used as sole variable explaining the upwash distribution, containing in it the effects of aircraft trim and vertical acceleration. After the treatment an inconclusive dependence of the vertical wind measurement on the aircraft's true airspeed remained. In-flight tests relate this dependence to an uncertainty of $0.06\,\mathrm{m\,s^{-1}}$ in the vertical wind measurement. As compared to ground measurements the final wind components were marginally underestimated by the aircraft ($\approx -0.1\,\mathrm{m\,s^{-1}}$).

Our findings emphasize that the 3-D wind vector can be measured reliably from a highly transportable and low-cost weight-shift microlight aircraft. Hence the necessary basis is provided for the study of precision and spectral quality of the wind measurement, which is prerequisite for reliable eddy-covariance flux measurements. This brings the weight-shift microlight aircraft platform an important step closer towards a fullfeatured environmental research aircraft.

Appendix A

Wind measurement transformation equations

The wind measurement from aircraft requires several coordinate systems, as well as angles to transform between them (Fig. 3). We define the wind vector $\boldsymbol{v}^{\mathrm{m}} = (v_{\mathrm{u}}^{\mathrm{m}}, v_{\mathrm{v}}^{\mathrm{m}}, v_{\mathrm{w}}^{\mathrm{m}})$ in the standard meteorological coordinate system (MCS, superscript m, positive eastward, northward, and upward). Then $\boldsymbol{v}^{\mathrm{m}}$ can be calculated from navigation, flow and attitude measurements: In the MCS $\boldsymbol{v}^{\mathrm{m}}$ is expressed as the vector difference between the aircraft's ground speed vector ($\boldsymbol{v}_{\mathrm{gs}}^{\mathrm{m}}$), directly measured by the inertial navigation system (INS), and the true airspeed vector ($\boldsymbol{v}_{\mathrm{tas^m}}$), essentially measured by the five hole probe (5HP, Williams and Marcotte, 2000):

$$\begin{aligned}\boldsymbol{v}^{\mathrm{m}} &= \boldsymbol{v}_{\mathrm{gs}}^{\mathrm{m}} - \boldsymbol{v}_{\mathrm{tas}}^{\mathrm{m}}\\ &= \boldsymbol{v}_{\mathrm{gs}}^{\mathrm{m}} - \mathbf{M}^{\mathrm{bm}} \times \left(\mathbf{M}^{\mathrm{ab}}(-v_{\mathrm{tas}}) + \boldsymbol{v}_{\mathrm{lev}}^{\mathrm{b}}\right). \qquad \text{(A1)}\end{aligned}$$

Yet the quantity directly measured by the 5HP is the true airspeed scalar v_{tas}. The second, decomposed form of the wind vector Eq. (A1) indicates that several calculation steps are necessary to arrive at the desired vector quantity $\boldsymbol{v}_{\mathrm{tas}}^{\mathrm{m}}$.

In the following we will walk through these successive steps, starting with the 5HP measurements. From the ports of the 5HP (Fig. 2) three differential pressures were measured:

$$p_{\mathrm{q,A}} = p_{\mathrm{t}} - p_{\mathrm{s}}, \qquad \text{(A2)}$$

$$p_{\alpha} = p_3 - p_1, \text{ and} \qquad \text{(A3)}$$

$$p_{\beta} = p_4 - p_2. \qquad \text{(A4)}$$

Measured dynamic pressure $p_{\mathrm{q,A}}$ (subscript upper-case letters A–G indicate calibration stage), and attack- and sideslip differential pressures p_{α}, p_{β} were used to calculate the airflow angles (Williams and Marcotte, 2000):

$$\alpha_{\mathrm{A}} = \frac{2}{9\sin(2\tau)}\frac{p_\alpha}{p_{\mathrm{q,A}}}, \text{ and} \tag{A5}$$

$$\beta_{\mathrm{A}} = \frac{2}{9\sin(2\tau)}\frac{p_\beta}{p_{\mathrm{q,A}}}. \tag{A6}$$

Here $\tau = 45^\circ$ is the angle between the central port p_t and the other ports p_1 through p_4 on the 5HP half sphere. Defining the normalization factor $D = \sqrt{1+\tan^2\alpha_{\mathrm{A}}+\tan^2\beta_{\mathrm{A}}}$ the measured dynamic pressure $p_{\mathrm{q,A}}$ can be corrected for the pressure drop occurring at elevated airflow angles:

$$p_{\mathrm{q,B}} = p_{\mathrm{q,A}}\left(\frac{9-5D^2}{4D^2}\right)^{-1}. \tag{A7}$$

Now we can derive v_{tas} from the thermodynamic measurements of the 5HP: Due to stagnation at the tip of the 5HP ambient air is heated from its intrinsic temperature (T_{s}) to total temperature (T_{t}). Assuming adiabatic heating, Bernoulli's equation

$$\begin{aligned} v_{\mathrm{tas}}^2 &= 2c_{\mathrm{p,h}}(T_{\mathrm{t}}-T_{\mathrm{s}}) \\ &= 2c_{\mathrm{p,h}}T_{\mathrm{s}}\left[\left(\frac{p_{\mathrm{s}}}{p_{\mathrm{s}}+p_{\mathrm{q}}}\right)^{-\kappa}-1\right], \end{aligned} \tag{A8}$$

gives v_{tas} as a function of the temperature difference (Leise and Masters, 1993). Since T_{t} can not be measured directly, it is substituted in Eq. (A8) by the adiabatic process (ram rise)

$$T_{\mathrm{t}} = T_{\mathrm{s}}\left(\frac{p_{\mathrm{s}}}{p_{\mathrm{s}}+p_{\mathrm{q}}}\right)^{-\kappa}, \tag{A9}$$

with the Poisson number $\kappa = 1 - \frac{c_{\mathrm{v,h}}}{c_{\mathrm{p,h}}}$. Furthermore the wind measurement should be independent of air humidity (subscript h). Therefore the specific heats under constant

pressure (subscript p) $c_{\mathrm{p,h}}$ or constant volume (subscript v) $c_{\mathrm{v,h}}$ of moist air have to be derived from the specific heat constants for dry air (subscript d) and water vapour (subscript w), $c_{\mathrm{p,d}} = 1005\,\mathrm{J\,kg^{-1}\,K^{-1}}$, $c_{\mathrm{p,w}} = 1846\,\mathrm{J\,kg^{-1}\,K^{-1}}$, $c_{\mathrm{v,d}} = 718\,\mathrm{J\,kg^{-1}\,K^{-1}}$, and $c_{\mathrm{v,w}} = 1384\,\mathrm{J\,kg^{-1}\,K^{-1}}$ (Khelif et al., 1999):

$$\begin{aligned} c_{\mathrm{p,h}} &= c_{\mathrm{p,d}}\left[1+q\left(\frac{c_{\mathrm{p,w}}}{c_{\mathrm{p,d}}}-1\right)\right], \\ c_{\mathrm{v,h}} &= c_{\mathrm{v,d}}\left[1+q\left(\frac{c_{\mathrm{v,w}}}{c_{\mathrm{v,d}}}-1\right)\right], \text{ with specific humidity being} \\ q &= \varepsilon\frac{e}{p_{\mathrm{s}}+e(\varepsilon-1)}, \end{aligned} \tag{A10}$$

where $\varepsilon = 0.622$ is the ratio of molecular weight of water vapour to that of dry air, and e is the 5HP measured water vapour pressure.

Once derived, the scalar quantity v_{tas} has to be transformed into a vector quantity. This can be achieved by defining the aerodynamic coordinate system (ACS, superscript a, positive forward, starboard, and downward), which has its origin at the 5HP tip. In this coordinate system the true airspeed vector has the components $\boldsymbol{v}_{\mathrm{tas}}^{\mathrm{a}} = (-v_{\mathrm{tas}}, 0, 0)$. Since the ACS is aligned with the streamlines its orientation however varies in time. Therefore $\boldsymbol{v}_{\mathrm{tas}}^{\mathrm{a}}$ is transformed into a fixed coordinate system, that is the trike body coordinate system (BCS, superscript b, positive forward, starboard, and downward) with its origin in the INS. This is accomplished by successive rotations about the vertical axis $\mathrm{Z^a}$ and the transverse axis $\mathrm{Y^a}$. Following Lenschow (1986) the rotations can be summarized in the operator

$$\mathbf{M}^{\mathrm{ab}} = D^{-1}\begin{pmatrix} 1 \\ \tan\beta \\ \tan\alpha \end{pmatrix}, \tag{A11}$$

with the 5HP derived airflow angles of attack α and sideslip β, and the normalization factor D as derived in Eqs. (A5)–(A7). Since $\boldsymbol{v}_{\mathrm{tas}^{\mathrm{a}}}$ carries all its information in the first vector component, it is sufficient to apply this transformation to $-v_{\text{tas}}$ in the wind vector Eq. (A1).

Now the wind vector is known in the orientation of the BCS, yet with its origin still at the 5HP tip as initially defined in the ACS. To allow for the vector difference as required in the wind Eq. (A1) we have to account for the displacement of ACS origin (5HP tip) relative to the BCS origin (INS). This is done by considering the lever arm correction vector (Williams and Marcotte, 2000):

$$\boldsymbol{v}^{\text{b}}_{\text{lev}} = \begin{pmatrix} \Omega^{\text{b}}_{\Phi} \\ \Omega^{\text{b}}_{\Theta} \\ \Omega^{\text{b}}_{\Psi} \end{pmatrix} \times \begin{pmatrix} x^{\text{b}} \\ y^{\text{b}} \\ z^{\text{b}} \end{pmatrix}, \tag{A12}$$

with INS measured body rates Ω^{b}_{Φ}, $\Omega^{\text{b}}_{\Theta}$, Ω^{b}_{Ψ} about the X^{b}, Y^{b}, Z^{b} axes, and the displacement of the 5HP with respect to the INS along these axes, $x^{\text{b}} = -0.73\,\text{m}$, $y^{\text{b}} = -0.01\,\text{m}$, and $z^{\text{b}} = 0\,\text{m}$. The vector sum $\mathbf{M}^{\text{ab}}(-v_{\text{tas}}) + \boldsymbol{v}^{\text{b}}_{\text{lev}}$ in the wind Eq. (A1) then describes the true airspeed vector in the BCS.

A last step remains to obtain $\boldsymbol{v}^{\text{m}}_{\text{tas}}$ for use in the wind Eq. (A1), that is the transformation of the true airspeed vector from the BCS into the MCS. This is achieved by a first transformation into the geodetic coordinate system (GCS, superscript g, positive northward, eastward and downward) via successive rotations about the X^{b}, Y^{b}, Z^{b} axes (Lenschow, 1986). From there the wind vector is permutated into the MCS (positive eastward, northward and upward). The transformations can be summarized in the operator

$$\mathbf{M}^{\text{bm}} = \begin{pmatrix} M^{\text{bm}}_{11} & M^{\text{bm}}_{12} & M^{\text{bm}}_{13} \\ M^{\text{bm}}_{21} & M^{\text{bm}}_{22} & M^{\text{bm}}_{23} \\ M^{\text{bm}}_{31} & M^{\text{bm}}_{32} & M^{\text{bm}}_{33} \end{pmatrix}, \quad \text{with} \tag{A13}$$

$$M^{\text{bm}}_{11} = \sin\Psi^{\text{b}}\cos\Theta^{\text{b}},$$

$$M^{\text{bm}}_{12} = \cos\Psi^{\text{b}}\cos\Phi^{\text{b}} + \sin\Psi^{\text{b}}\sin\Phi^{\text{b}}\sin\Theta^{\text{b}},$$
$$M^{\text{bm}}_{13} = \sin\Psi^{\text{b}}\sin\Theta^{\text{b}}\cos\Phi^{\text{b}} - \cos\Psi^{\text{b}}\sin\Phi^{\text{b}},$$
$$M^{\text{bm}}_{21} = \cos\Psi^{\text{b}}\cos\Theta^{\text{b}},$$
$$M^{\text{bm}}_{22} = \cos\Psi^{\text{b}}\sin\Theta^{\text{b}}\sin\Phi^{\text{b}} - \sin\Psi^{\text{b}}\cos\Phi^{\text{b}},$$
$$M^{\text{bm}}_{23} = \sin\Psi^{\text{b}}\sin\Phi^{\text{b}} + \cos\Psi^{\text{b}}\sin\Theta^{\text{b}}\cos\Phi^{\text{b}},$$
$$M^{\text{bm}}_{31} = \sin\Theta^{\text{b}},$$
$$M^{\text{bm}}_{32} = -\cos\Theta^{\text{b}}\sin\Phi^{\text{b}},$$
$$M^{\text{bm}}_{33} = -\cos\Theta^{\text{b}}\cos\Phi^{\text{b}},$$

where Φ^{b}, Θ^{b}, and Ψ^{b} are the INS measured attitude angles roll, pitch and heading, respectively. Finally the movement of the BCS with respect to the MCS is described by $\boldsymbol{v}^{\text{m}}_{\text{gs}}$ in the wind vector Eq. (A1).

Appendix B Uncertainty quantification

B1 Uncertainty propagation

In Eq. (A1) the wind vector is the difference between the aircraft's ground speed vector ($\boldsymbol{v}^{\text{m}}_{\text{gs}}$) and the true airspeed vector ($\boldsymbol{v}^{\text{m}}_{\text{tas}}$). The measurement of $\boldsymbol{v}^{\text{m}}_{\text{gs}}$ is readily provided by the inertial navigation system, together with the related uncertainty (Table 2). Uncertainty propagation is however required for $\boldsymbol{v}^{\text{m}}_{\text{tas}}$, since 12 measured quantities are merged during its calculation. The magnitude of the lever arm correction Eq. (A12), and with it possible uncertainty from this source, is two orders lower than $\boldsymbol{v}^{\text{m}}_{\text{tas}}$. It can therefore be neglected in the uncertainty propagation, which leaves nine measured quantities. By preprocessing Eqs. (A5)–(A10) these are further condensed to three measured quantities and three derived variables (see next paragraph for respective uncertainty propagation). Modified after Vörsmann (1985) the input uncertainty of the $\boldsymbol{v}^{\mathrm{m}}_{\mathrm{tas}}$ measurement can then be calculated from a linearised uncertainty propagation model in the vector components $v^{\mathrm{m}}_{\mathrm{tas,c}}$ (c = u, v, or w):

$$\Delta v^{\mathrm{m}}_{\mathrm{tas,c}} = \sum_{i=1}^{i=6} \left| \frac{\delta v^{\mathrm{m}}_{\mathrm{tas,c}}}{\delta f_i} \, \sigma(f_i) \right|, \tag{B1}$$

with $\frac{\delta v^{\mathrm{m}}_{\mathrm{tas,c}}}{\delta f_i}$ being the partial derivatives of Eqs. (A11) and (A13) inserted into the wind vector Eq. (A1). Thereby the input uncertainty of $\boldsymbol{v}^{\mathrm{m}}_{\mathrm{tas}}$ can be expressed as function of the (assumed independent) input variables (f_i), with $\sigma(f_i)$ being their respective uncertainty. Here f_i are three quantities directly measured by the INS (i.e. pitch- (Θ^{b}), roll- (Φ^{b}) and heading- (Ψ^{b}) angles) and three variables derived from five hole probe measurements (i.e. attack angle (α), sideslip angle (β) and true airspeed scalar (v_{tas})). Such a procedure is conservative, since it assumes uncertainty interference, but not cancellation. It yields the maximum possible uncertainty triggered by the combined effects of σf_i. The derivatives were further simplified by small-angle approximation. This simplification allows to express the input uncertainty with sign and sensitivity as a function of Ψ^{b}, whereas the full form yields the maximum absolute input uncertainty for different flight states.

In analogy uncertainty propagation models were formulated for the three derived variables α in Eq. (A5), β in Eq. (A6) and v_{tas} in Eq. (A8). These permit to express the actual uncertainties originating from the six remaining directly measured quantities, i.e. both flow angle differential pressures, dynamic- and static pressures, static temperature, and water vapour pressure.

With this setup the overall uncertainty at each stage of the wind calculation procedure can be evaluated through Gaussian uncertainty propagation (e.g., Taylor, 1997):

$$\sigma_{\mathrm{gau}} = \sqrt{\sum_{i=1}^{N} \sigma_i^2}, \tag{B2}$$

with N being the number of (assumed linear and independent) uncertainty terms contributing to the stage investigated.

B2 Uncertainty measures

For applications in the atmospheric boundary layer the comparison to a reference standard can yield an integral measure of confidence under varying conditions (e.g., Vogt and Thomas, 1995; Mauder et al., 2006). Therefore this study employs two basic bivariate criteria for the comparison of wind components. These are the root mean square deviation (RMSD) and bias (BIAS) between sample and reference (ISO, 1993):

$$\mathrm{RMSD} = \sqrt{\frac{1}{N} \sum_{i=1}^{N} (A_i - R_i)^2}, \tag{B3}$$

$$\mathrm{BIAS} = \frac{1}{N} \sum_{i=1}^{N} (A_i - R_i), \tag{B4}$$

with N being the number of data couples R_i and A_i, R_i being the ith reference observation and A_i the ith observation by aircraft sensors, sampled simultaneously. RMSD is also called comparability and is a measure of overall uncertainty. BIAS is the systematic difference between the mean of the measurements and the reference. These criteria were not normalized, since no consistent dependence on the wind magnitude or the aircraft's true airspeed was found.

Appendix C Notation

Scalars and vector components are displayed in italics, vectors are displayed in bold italics, and matrices are displayed in bold roman typeface, respectively. Where applicable coordinate systems and respective axes are indicated by superscripts, whereas subscripts are used as specifiers.

C1 Operators

$[\mathbf{M}]$	Transformation matrix
$[\delta]$	Differential operator
$[\Delta]$	Difference operator

C2 Parameters and variables

a	Acceleration
A	Aircraft measurement
BIAS	Bias
CL	Lift coefficient
c_p	Specific heat at constant pressure
c_v	Specific heat at constant volume
D	Derived term containing airflow angles
f	Place-holder for input variables
g	Gravitational acceleration
i	Continuous index
L	Lift
LF	Loading factor
$\frac{L}{S}$	Wing loading
m	Mass
n	Normalized centre of pressure – 5HP separation distance
N	Sample size
p	Pressure
q	Specific humidity
R	Reference measurement
RMSD	Root mean square deviation
S	Wing surface area
T	Temperature

v	Velocity scalar or vector component
$\boldsymbol{v}$	Velocity vector
$x,\ y,\ z$	Distances on respective coordinate axes
$\frac{z}{L}$	Stability parameter
α	Angle of attack
β	Angle of sideslip
ε	Ratio of molecular masses
Θ	Pitch
κ	Poisson number
Φ	Roll
ξ	Upwash attack angle
π	Perimeter constant
ρ	Air density
σ	Standard deviation, RMSD
τ	Angle between central and surrounding ports on half-sphere
Ψ	Heading
Ω	Body rate

C3 Subscripts – superscripts

1–4	Pressure ports
∞	Free airstream
$+,-$	Into wind, with wind
$\tilde{}$	Wind tunnel
a	Aerodynamic coordinate system, positive forward, starboard, and downward
A–G	Calibration steps
b	Body coordinate system, positive forward, starboard and downward
d	Dry air
g	Geodetic coordinate system, positive northward, eastward and downward

gau	Gaussian uncertainty propagation
gs	Ground speed
h	Humid air
lev	Lever arm
m	Meteorological coordinate system, positive eastward, northward and upward
off	Offset
q	Dynamic-
r	Inverse reference
s	Static-
slo	Slope
t	Total-
tas	True airspeed
u, v, w	Wind components in x, y, z directions
up	Upwash
w	Water vapour; Wing coordinate system, positive forward, starboard and downward
x, y, z	Standard Cartesian coordinate axes
α	Angle of attack
β	Angle of sideslip

C4 Abbreviations

5HP	Five hole probe
ABL	Atmospheric boundary layer
ACS	Aerodynamic coordinate system, positive forward, starboard, and downward
a.g.l.	Above ground level
a.s.l.	Above sea level
BCS	Body coordinate system, positive forward, starboard and downward
D-MIFU	Name of aircraft
DAQ	Data acquisition
E	East
EC	Eddy covariance
EIDAS	Embedded Institute for Meteorology and Climate Research data acquisition system
FWA	Fixed-wing aircraft
GCS	Geodetic coordinate system, positive northward, eastward and downward
INS	Inertial navigation system
IU	Input uncertainty
LI	Lindenberg
MCS	Meteorological coordinate system, positive eastward, northward and upward
N	North
S	South
ST	Lake Starnberg
ULS	Universal laser sensor
VW1–VW3	Vertical wind specific flight patterns
W	West
WCS	Wing coordinate system, positive forward, starboard and downward
WSMA	Weight-shift microlight aircraft
XI	Xilinhot

Acknowledgements. Special recognition has to be given to Josef-Michael Burger, Matthias Mauder, Frank Neidl, Rainer Steinbrecher and Rose Zuurbier at the Karlsruhe Institute of Technology, Institute for Meteorology and Climate Research. Burger and Zuurbier carried out the bulk of the wind-tunnel measurements, whereas Mauder contributed his invaluable micrometeorological advise. Neidl programmed and continuously maintained the data acquisition system, while Steinbrecher initiated wind- and flux measurements with the weight-shift microlight aircraft in the first place. Our gratefulness to Xunhua Zheng and her work-group at the Chinese Academy of Sciences, Institute of Atmospheric Physics, who was hosting our project and providing indispensable infrastructure. We are much obliged to Frank Beyrich of the German Meteorological Service, Richard-Aßmann-Observatory, who permitted us to carry out the evaluation flights and provided us with the corresponding SODAR- and tower data for this study. Our thanks to Jens Bange and Aline van den Kroonenberg of the Technical University of Braunschweig, Institute of Aerospace Systems (now Eberhard Karls University of Tübingen, Institute for Geoscience), for their tireless advise. Stipend funding by the German Academic Exchange Service, Helmholtz Association of German Research Centres, China Scholarship Council and the European Union under the Science and Technology Fellowship China is acknowledged. The flight in Inner Mongolia was funded by the German Research Foundation, research group 536 “Matter fluxes in grasslands of Inner Mongolia as influenced by stocking rate”.

References

Baldocchi, D., Falge, E., Gu, L., Olson, R., Hollinger, D., Running, S., Anthoni, P., Bernhofer, C., Davis, K., Evans, R., Fuentes, J., Goldstein, A., Katul, G., Law, B., Lee, X., Malhi, Y., Meyers, T., Munger, W., Oechel, W. U. K., Pilegaard, K., Schmid, H., Valentini, R., Verma, S., Vesala, T., Wilson, K., and Wofsy, S.: FLUXNET: A new tool to study the temporal and spatial variability of ecosystem-scale carbon dioxide, water vapor, and energy flux densities, B. Am. Meteorol. Soc., 82, 2415–2434, 2001. 1305

Bange, J. and Roth, R.: Helicopter-borne flux measurements in the nocturnal boundary layer over land – a case study, Bound.-Lay. Meteorol., 92, 295–325, 1999. 1308

Beyrich, F., Leps, J. P., Mauder, M., Bange, J., Foken, T., Huneke, S., Lohse, H., Ludi, A., Meijninger, W. M. L., Mironov, D., Weisensee, U., and Zittel, P.: Area-averaged surface fluxes over the litfass region based on eddy-covariance measurements, Bound.-Layer Meteorol., 121, 33–65, 2006. 1305

Bissolli, P. and Dittmann, E.: The objective weather type classification of the German Weather Service and its possibilities of application to environmental and meteorological investigations, Meteorol. Z., 10, 253–260, 2001. 1354

Bohn, D. and Simon, H.: Mehrparametrige Approximation der Eichräume und Eichflächen von

Unterschall- bzw. Überschall-5-Loch-Sonden, Archiv für Technisches Messen und Meßtechnische Praxis, 470, 31–37, 1975. 1324

Boiffier, J.-L.: The Dynamics of Flight: The Equations, Wiley, 1998. 1314

Brown, E. N., Friehe, C. A., and Lenschow, D. H.: The use of pressure-fluctuations on the nose of an aircraft for measuring air motion, J. Clim. Appl. Meteorol., 22, 171–180, 1983. 1305

Cook, M. V.: The theory of the longitudinal static stability of the hang-glider, Aeronaut. J., 98, 292–304, 1994. 1308

Cook, M. V. and Spottiswoode, M.: Modelling the flight dynamics of the hang glider, Aeronaut. J., 110, 1–20, 2006. 1308

Cooper, W. A. and Rogers, D.: Effects of air-flow trajectories around aircraft on measurements of scalar fluxes, J. Atmos. Ocean. Tech., 8, 66–77, 1991. 1309

Crawford, T. L. and Dobosy, R. J.: A sensitive fast-response probe to measure turbulence and heat-flux from any airplane, Bound.-Lay. Meteorol., 59, 257–278, 1992. 1305, 1306, 1311, 1324

Crawford, T., Dobosy, R., and Dumas, E.: Aircraft wind measurement considering lift-induced upwash, Bound.-Layer Meteorol., 80, 79–94, 1996. 1305, 1309, 1310, 1320, 1327

Desjardins, R. L., MacPherson, J. I., Mahrt, L., Schuepp, P., Pattey, E., Neumann, H., Baldocchi, D., Wofsy, S., Fitzjarrald, D., McCaughey, H., and Joiner, D. W.: Scaling up flux measurements for the boreal forest using aircraft-tower combinations, J. Geophys. Res., 102, 29125–29133, 1997. 1305

Egger, J., Bajrachaya, S., Heinrich, R., Kolb, P., Lammlein, S., Mech, M., Reuder, J., Schaper, W., Shakya, P., Schween, J., and Wendt, H.: Diurnal winds in the Himalayan Kali Gandaki valley. Part III: Remotely piloted aircraft soundings, Mon. Weather Rev., 130, 2042–2058, 2002. 1305

Foken, T.: Temperaturmessungen mit dünnen Platindrähten, Z. Meteorol., 29, 299–307, 1979. 1322

Foken, T. and Wichura, B.: Tools for quality assessment of surface-based flux measurements, Agr. Forest Meteorol., 78, 83–105, 1996. 1319, 1324

Garman, K. E., Hill, K. A., Wyss, P., Carlsen, M., Zimmerman, J. R., Stirm, B. H., Carney, T. Q., Santini, R., and Shepson, P. B.: An airborne and wind tunnel evaluation of a wind turbulence measurement system for aircraft-based flux measurements, J. Atmos. Ocean. Tech., 23, 1696–1708, 2006. 1306

Garman, K. E., Wyss, P., Carlsen, M., Zimmerman, J. R., Stirm, B. H., Carney, T. Q., Santini, R., and Shepson, P. B.: The contribution of variability of lift-induced upwash to the uncertainty in vertical winds determined from an aircraft platform, Bound.-Lay. Meteorol., 126, 461–476, 2008. 1305, 1309, 1327

Gratton, G. B.: The weightshift-controlled microlight aeroplane, Proceedings of the Institution of Mechanical Engineers Part G, J. Aerospace Eng., 215, 147–154, 2001. 1308

Hobbs, S., Dyer, D., Courault, D., Olioso, A., Lagouarde, J. P., Kerr, Y., McAneney, J., and Bonnefond, J.: Surface layer profiles of air temperature and humidity measured from unmanned aircraft, Agronomie, 22, 635–640, 2002. 1305

ISO: Statistics – vocabulary and symbols – Part 1: Probability and general statistical terms, vol. ISO 3534-1, International Organization for Standardization, Geneva, Switzerland, 1993. 1342

Junkermann, W.: An ultralight aircraft as platform for research in the lower troposphere: system performance and first results from radiation transfer studies in stratiform aerosol layers and broken cloud conditions, J. Atmos. Ocean. Tech., 18, 934–946, 2001. 1305, 1307

Junkermann, W.: The actinic UV-radiation budget during the ESCOMPTE campaign 2001: results of airborne measurements with the microlight research aircraft D-MIFU, Atmos. Res., 74, 461–475, 2005. 1305

Kaimal, J. and Finnigan, J.: Atmospheric Boundary Layer Flows: Their Structure and Measurement, Oxford University Press, 1994. 1306

Kalogiros, J. A. and Wang, Q.: Calibration of a radome-differential GPS system on a twin otter research aircraft for turbulence measurements, J. Atmos. Ocean. Tech., 19, 159–171, 2002a. 1305, 1306, 1317

Kalogiros, J. A. and Wang, Q.: Aerodynamic effects on wind turbulence measurements with research aircraft, J. Atmos. Ocean. Tech., 19, 1567–1576, 2002b. 1305, 1327

Khelif, D., Burns, S. P., and Friehe, C. A.: Improved wind measurements on research aircraft, J. Atmos. Ocean. Tech., 16, 860–875, 1999. 1306, 1317, 1338

van den Kroonenberg, A., Martin, T., Buschmann, M., Bange, J., and Vorsmann, P.: Measuring the wind vector using the autonomous mini aerial vehicle M2AV, J. Atmos. Ocean. Tech., 25, 1969–1982, 2008. 1305, 1313, 1319

Leise, J. A. and Masters, J. M.: Wind measurement from aircraft, Tech. rep., United States Department of Commerce, National Oceanic and Atmospheric Administration, Aircraft Operations Center, MacDill Air Force Base, 1993. 1311, 1316, 1337

Lenschow, D. H.: Aircraft measurements in the boundary layer, in: Probing the Atmospheric

Boundary Layer, American Meteorological Society, Boston, Massachusetts, USA, 39–55, 1986. 1305, 1318, 1329, 1338, 1339

Mauder, M., Liebethal, C., Gockede, M., Leps, J. P., Beyrich, F., and Foken, T.: Processing and quality control of flux data during LITFASS-2003, Bound.-Lay. Meteorol., 121, 67–88, 2006. 1342

Mauder, M., Desjardins, R. L., and MacPherson, I.: Creating surface flux maps from airborne measurements: application to the Mackenzie area GEWEX study MAGS 1999, Bound.-Lay. Meteorol., 129, 431–450, 2008. 1305

Taylor, J. R.: An Introduction to Error Analysis: the Study of Uncertainties in Physical Measurements, University Science Books, Mill Valley, California, USA, 2nd edn., 1997. 1341

Tjernström, M. and Friehe, C. A.: Analysis of a radome air-motion system on a twin-jet aircraft for boundary-layer research, J. Atmos. Ocean. Tech., 8, 19–40, 1991. 1306, 1313, 1317, 1329

Trenkle, F. and Reinhardt, M.: In-flight temperature measurements, vol. 2 of Advisory Group for Aerospace Research and Development: Flight Test Instrumentation Series, North Atlantic Treaty Organization, Neuilly-sur-Seine, France, 1973. 1322

Visbal, M. R. and Shang, J. S.: Investigation of the flow structure around a rapidly pitching airfoil, AIAA J., 27, 1044–1051, 1989. 1334

Vogt, S. and Thomas, P.: Sodar – a useful remote sounder to measure wind and turbulence, J. Wind Eng. Ind. Aerod., 54, 163–172, 1995. 1342

Vörsmann, P.: Ein Beitrag zur Bordautonomen Windmessung, Ph.D. thesis, Technische Universität Braunschweig, 1985. 1341

Williams, A. and Marcotte, D.: Wind measurements on a maneuvering twin-engine turboprop aircraft accounting for flow distortion, J. Atmos. Ocean. Tech., 17, 795–810, 2000. 1306, 1313, 1316, 1336, 1337, 1339

Wyngaard, J. C.: The effects of probe-induced flow distortion on atmospheric-turbulence measurements, J. Appl. Meteorol., 20, 784–794, 1981. 1309

Table 1. Overview of sensors and electronic instrumentation used for the wind measurement.

Component	Model	Manufacturer	Address
Butterworth low pass filter	AF40-4BU TP	E.S.F. electronic	Göttingen, Germany
Electronic compass module	TCM2-20	PNI Sensor Corporation	Santa Rosa, USA
Humidity sensor	SHT75	Sensirion AG	Staefa, Switzerland
Industrial computer	PR-Z32-EA-ST	Diamond Systems Corporation	Newark, USA
Inertial navigation system	RT3102	Oxford Technical Solutions	Upper Heyford, England
Pressure sensor	PCLA12X5D	Sensortechnics GmbH	Puchheim, Germany
Pressure sensor	SP82AL	Capto As.	Horten, Norway
Thermocouple	CHAL-002	OMEGA Engineering, Inc.	Stamford, USA
Three-axis accelerometer	ADXL330	Analog Devices, Inc.	Norwood, USA
Universal laser sensor	ULS (Second edition)	Laser Technology, Inc.	Centennial, USA
Operating system	Minix 2.0	Andrew Stuart Tanenbaum	Amsterdam, Netherlands

Table 2. List of measured variables, sensor characteristics, signal processing and data acquisition. Individual sensor locations are described in Sect. 2.2 and displayed in Figs. 1 and 2. Resolution refers to the smallest change registered by the data acquisition (DAQ) units. σ is the overall sensor uncertainty provided by the manufacturer in form of one standard deviation. Signal rates are displayed for sampling, filtering and storing (Signal SFS). Data acquisition takes place in two forms, standalone (SA) and on the central DAQ unit EIDAS. For non SA devices signal forwarding via A/D converter, recommended standard 232 (RS232) or serial peripheral interface (SPI) is indicated (Interface DAQ). Continued on next page.

Quantity	Variable	Sensor	Range	Resolution	σ	Signal SFS [s^{-1}]		Interface DAQ	
Airframe motion									
Latitude/longitude		RT3102	$\pm 89.9^\circ / \pm 180^\circ$	$6 \times 10^{-15\circ}$	1.1 m	100	100		SA
Altitude sea level		RT3102	< 18000 m	0.001 m	2.7 m	100	100		SA
Altitude ground level		ULS	0.15–500 m	0.001 m	0.04 m	10	10	RS232	EIDAS
Heading, body	Ψ^b	RT3102	0–360°	0.00006°	0.1°	100	100		SA
Heading, wing	Ψ^w	TCM2-20	0–360°	0.1°	0.5°	16	10	RS232	EIDAS
Pitch/roll, body	Θ^b / Φ^b	RT3102	$\pm 90^\circ / \pm 180^\circ$	0.00006°	0.06°	100	100		SA
Pitch/roll, wing	Θ^w / Φ^w	TCM2-20	±20°	0.1°	0.2°	16	10	RS232	EIDAS
3-D velocity, body	v_{gs}^m	RT3102	0–515 $m\,s^{-1}$	0.0001 $m\,s^{-1}$	0.02 $m\,s^{-1}$	100	100		SA
3-D ang. rat., body	Ω^b	RT3102	$\pm 100^\circ\,s^{-1}$	$0.0006^\circ\,s^{-1}$	$0.01^\circ\,s^{-1}$	100	100		SA
3-D accel., body	a^b	RT3102	±10 g	0.00001 g	0.001 g	100	100		SA
3-D accel., wing		ADXL330	±3 g	0.0003 g	0.01 g	100	100	A/D	EIDAS
3-D accel., 5HP		ADXL330	±3 g	0.0003 g	0.01 g	100	100	A/D	EIDAS

Table 2. Continued.

Quantity	Variable	Sensor	Range	Resolution	σ	Signal SFS [s^{-1}]			Interface	DAQ
Relative air motion										
Static pressure	$p_{s,A}$	SP82AL	0–1000 hPa	0.02 hPa	0.1 hPa	100	20	10	A/D	EIDAS
Dynamic pressure	$p_{q,A}$	PCLA12X5D	±12.5 hPa	0.0005 hPa	0.06 hPa	100	20	10	A/D	EIDAS
Attack pressure	p_α	PCLA12X5D	±12.5 hPa	0.0005 hPa	0.06 hPa	100	20	10	A/D	EIDAS
Sideslip pressure	p_β	PCLA12X5D	±12.5 hPa	0.0005 hPa	0.06 hPa	100	20	10	A/D	EIDAS
Fast temp.	T_s	CHAL-002	−20–60 °C	0.0015 K	0.5 K	100	20	10	A/D	EIDAS
Humidity, 5HP	e	SHT75	0–70 hPa	0.07 hPa	0.3 hPa	10		10	SPI	EIDAS
DAQ synchronization										
GPS time		RT3102		0.001 s	0.001 s	100		100		SA
GPS time		RT3102		0.1 s	0.1 s	100		10	RS232	EIDAS

Table 3. Flight campaign summary, respective locations are Lake Starnberg (ST), Lindenberg (LI), and Xilinhot (XI). Synoptic wind direction and cyclonality (CYC) were retrieved from the objective weather type data base of the German Meteorological Service (Bissolli and Dittmann, 2001). The XI flight on 31 July 2009 was supplemented with publicly available data from the US National Centre for Environmental Prediction. Prevailing wind direction throughout all flight days was south-west, anticyclonic and cyclonic conditions are indicated by a and c, respectively. Sea level pressure (p), 2 m a.g.l. maximum temperature (T_{max}) and cloud coverage are 24 h observations of the closest national meteorological service station on the respective day. For the flight patterns racetrack (RACE), wind square (SQUA), variance optimization (VARI), vertical wind specific flights (VW1–VW3) and the comparison to ground based measurements (COMP) the number of available datasets for each date is given together with respective track length (km) in parenthesis.

Date	19 Jun 2008	24 Jun 2008	25 Jun 2008	11 Jul 2008	15 Oct 2008	16 Oct 2008	18 Oct 2008	20 Oct 2008	21 Oct 2008	31 Jul 2009
Location	ST	ST	ST	ST	LI	LI	LI	LI	LI	XI
CYC 950 hPa	a	a	c	c	a	c	a	a	c	a
CYC 500 hPa	a	a	a	a	a	c	a	a	a	a
p [hPa]	1019	1021	1020	1015	1017	1008	1020	1018	1012	1010
T_{max} [°C]	22.4	21.6	27.7	27.8	14.8	14.3	13.1	16.5	21.7	31.1
Cloud cover	5/8	4/8	4/8	4/8	8/8	8/8	5/8	4/8	4/8	7/8
RACE	2 (10)	4 (10)	4 (10)				4 (10)			
SQUA		5 (12)	1 (12)							
VARI								6 (20)	4 (20)	2 (80)
VW1			1 (4)							
VW2		1 (11)	1 (11)							
VW3			1 (9)							
COMP					6 (12)	5 (12)	6 (12)			

Table 4. Coefficients for static pressure (p_s), dynamic pressure (p_q), differential pressures (p_α, p_β), static temperature (T_s), and flow angle measurements (α, β) during calibration steps A–G. Respective environments are laboratory (LAB), wind tunnel (TUN), comparison to ground based measurements (COMP), racetrack (RACE), wind square (SQUA), variance optimization (VARI) and vertical wind (VW) specific flight patterns. Coefficients are distinguished in offset (off) and slopes (slo), where applicable with lift coefficient in the upwash corrections (upw). Cross-calibration is referred to with the calibration steps in parentheses. Coefficients in parentheses were only used for intermediate calculations.

Variable	Coefficient	A. LAB	B. TUN	C. COMP	D. RACE	E. SQUA	F. VARI	G. VW
p_s	off [hPa]	−1.220		−2.26				
	slo [–]	225.170						
p_q	off [hPa]	−13.895	0.216					
	slo [–]	6.068	1.049		1.085			
p_α	off [hPa]	−13.706						
	slo [–]	6.088						
p_β	off [hPa]	−13.704						
	slo [–]	6.060						
T_s	off [K]	−33.821						
	slo [–]	9.762						
α	upw,off [rad]					(0.005)	(0.017)	0.039 (F)
	upw,slo [rad]							−0.027
	slo [–]							1(F)
β	upw,off [rad]					(−0.012)	(−0.014)	−0.004 (E)
	upw,slo (rad)							−0.010 (E)
	slo [–]							1(F)

Table 5. Uncertainty of variables entering the wind vector computation Eq. (A1): Static pressure (p_s), dynamic pressure as used in the computation of flow angles ($p_{q,A}$) and the true airspeed ($p_{q,B}$), differential pressures (p_α, p_β), static temperature (T_s) and water vapour pressure (e). Sources of uncertainty (σ) are subscripted as follows: manufacturer provided sensor uncertainty (sen), calibration in laboratory (lab), wind tunnel (tun), and wind model description (mod). The 0.05 K and 0.36 K uncertainties for radiation and ram rise errors in static temperature (T_s) were accounted in σ_{mod}. These input uncertainties were Gaussian summarized ($\sigma_{gau,i}$) and propagated into output uncertainties (σ) of attack angle (α), sideslip angle (β) and true airspeed (v_{tas}), using the sensitivities (S) in their respective computations Eqs. (A5), (A6), and (A8). Propagated output uncertainties were summed up in analogy to Eq. (B1) before Gaussian summarizing them with the non-propagated uncertainties for α and β wind tunnel measurements to the final output uncertainties ($\sigma_{gau,o}$).

Variable				Input				Sensitivities			Output	
	Unit x	σ_{sen} $[x]$	σ_{lab} $[x]$	σ_{tun} $[x]$	σ_{mod} $[x]$	$\sigma_{gau,i}$ $[x]$	S_α $[°/x]$	S_β $[°/x]$	$S_{v_{tas}}$ $[ms^{-2}/x]$	σ_α [°]	σ_β [°]	$\sigma_{v_{tas}}$ $[ms^{-1}]$
Propagated												
p_s	[hPa]	0.10	0.58			0.59			−0.01			0.01
$p_{q,A}$	[hPa]	0.06	0.03			0.07	4.26	3.60		0.29	0.24	
$p_{q,B}$	[hPa]	0.06	0.03	0.04		0.08			3.85			0.30
p_α	[hPa]	0.06	0.03			0.07	4.57	0.97		0.31	0.07	
p_β	[hPa]	0.06	0.03			0.07	0.48	4.74		0.03	0.32	
T_s	[K]	0.26	0.40		0.36	0.60			0.04			0.02
e	[hPa]	0.30				0.30			0.01			
$\sum$										0.62	0.62	0.34
Non-propagated												
α	[°]			0.44		0.44	1.00			0.44		–
β	[°]			0.43		0.43		1.00			0.43	–
$\sigma_{gau,o}$										0.76	0.76	0.34

Table 6. Input uncertainty (IU) from the linear uncertainty propagation model Eq. (B1). For the sensitivity analysis the model was forced with two different reference states, State 1 with small and State 2 with enhanced flow (α, β) and attitude (Θ^b, Φ^b, Ψ^b,) angles. Both states were inferred similar uncertainty quantities Δf_i in α, β, Θ^b, Φ^b, Ψ^b, and true airspeed (v_{tas}). State 1 allows for the small-angle approximation in Eq. (B1), resulting in uncertainties for the wind components (Δv^m_{uvw}) as a function of the heading angle (Ψ). The full form of Eq. (B1) must however be used for State 2. It allows to calculate the maximum uncertainty in the wind components ($|\Delta v^m_{uvw}|$) over all Ψ, as well as to compare these between both flight states. After calibration step B the reference State 2 was used for the uncertainty propagation: the actual uncertainties in a) the flow computation (α, β and v_{tas}, Table 5), and b) the sensor alignment (Θ^b, Φ^b, Ψ^b) were inferred. This allows to estimate the wind measurements uncertainty constraint by sensor setup and wind model description.

Variable	α	β	Θ^b	Φ^b	Ψ^b	v_{tas}	IU
Model forcing							
State 1	1°	1°	1°	1°	0…360°	$27\,m\,s^{-1}$	
State 2	−15°	−15°	10°	10°	0…360°	$27\,m\,s^{-1}$	
$\Delta f_{i,sensitivity}$	1°	1°	1°	1°	1°	$0.5\,m\,s^{-1}$	
$\Delta f_{i,propagation}$	0.76°	0.76°	0.1°	0.1°	0.1°	$0.34\,m\,s^{-1}$	
Results State 1 – sensitivity							
Δv^m_u [$m\,s^{-1}$]	< 0.01	0.47cosΨ	< 0.01	< 0.01	0.47cosΨ	0.50	1.08
Δv^m_v [$m\,s^{-1}$]	< 0.01	−0.47sinΨ	< 0.01	< 0.01	−0.47sinΨ	0.50	1.08
Δv^m_w [$m\,s^{-1}$]	0.47	< 0.01	−0.47	< 0.01	< 0.01	< 0.01	0.95
$\|\Delta v^m_{uv}\|$ [$m\,s^{-1}$]	0.01	0.47	< 0.01	0.01	0.47	0.5	1.08
$\|\Delta v^m_w\|$ [$m\,s^{-1}$]	0.47	0.01	0.48	0.01	0.00	< 0.01	0.97
Results State 2 – sensitivity							
$\|\Delta v^m_{uv}\|$ [$m\,s^{-1}$]	0.21	0.47	0.21	0.14	0.42	0.45	1.34
$\|\Delta v^m_w\|$ [$m\,s^{-1}$]	0.41	0.05	0.32	0.14	0.00	0.22	1.14
Results State 2 – propagation							
$\|\Delta v^m_{uv}\|$ [$m\,s^{-1}$]	0.16	0.36	0.02	0.01	0.04	0.30	0.64
$\|\Delta v^m_w\|$ [$m\,s^{-1}$]	0.31	0.04	0.03	0.01	0.00	0.15	0.55

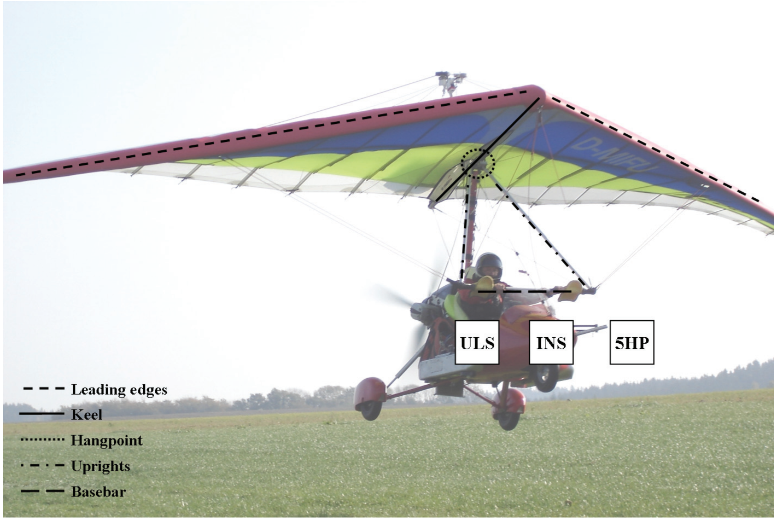

Fig. 1. Weight-shift microlight research aircraft D-MIFU, aircraft structural features are highlighted by dash-dotted lines. Sensor locations of five hole probe (5HP), inertial navigation system (INS, inside aircraft nose) and universal laser sensor (ULS, below pilot seat) are indicated. For details on the respective installations see Sect. 2.2 and Table 2. Figure 2 details the layout of the five hole probe.

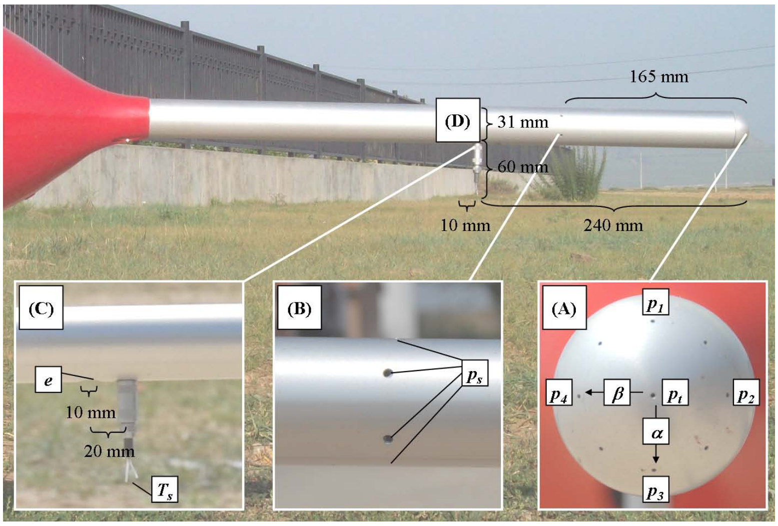

Fig. 2. Layout of the five hole probe, with letters indicating sensor locations. **(A)** The tip of the five hole probe is designed as a half sphere, with a total pressure (p_t) port at its centre. Two additional pressure ports on each, the vertical (p_1, p_3) and the horizontal axis (p_2, p_4), surround the central port at an angle of $\tau = 45°$. These differential pressure readings are used to determine attack angle (α) and sideslip angle (β), respectively, arrows indicate the direction of positive angular measurement. Additional (unnumbered) pressure ports at 45° increments are not used in this study. **(B)** Six pressure ports downstream of the half sphere are ring-compensated around the circumference of the five hole probe for flow angle independent static pressure (p_s) measurement. **(C)** Freely suspended 50 µm thermocouple for fast temperature (T_s) measurement and 10 mm port for the capacitive humidity measurement (e). **(D)** Location of five hole probe 3-D acceleration sensor. The whole installation weights in at 350 g.

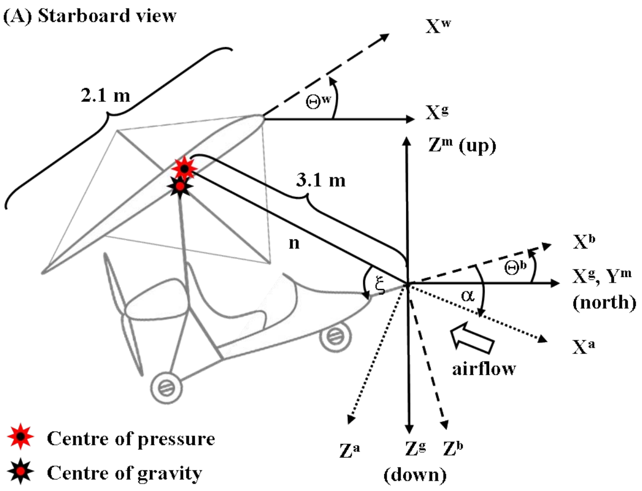

Fig. 3. Geometrical features of the weight-shift microlight aircraft and coordinate systems with axes X, Y, and Z used to compute the wind vector. The superscripts a, b, g, m and w represent, respectively, the aerodynamic-, body-, geodetic-, meteorological and wing coordinate systems (Appendix A). **(A)** Starboard view: Angle of attack (α), pitch angle (Θ), centre of gravity and centre of pressure. Relating the distance between five hole probe measurement and centre of pressure (3.1 m) to the wing's chord length (2.1 m) results in the normalized radius about the centre of pressure (n), enclosing the upwash attack angle (ξ) with the body X-axis (X^b). Continued on next page: **(B)** Rear view: Roll angle (Φ); **(C)** Top view: Sideslip angle (β) and true heading (Ψ). Since trike and wing are fixed in the longitudinal axis Ψ is not duplicated. In addition the distances between five hole probe measurement and the inertial navigation system (0.7 m) and propeller (3.5 m) as well as the wing's chord length (2.1 m) is shown.

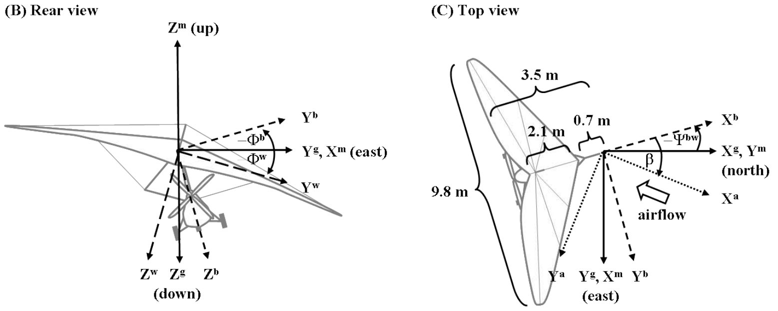

Fig. 3. Continued.

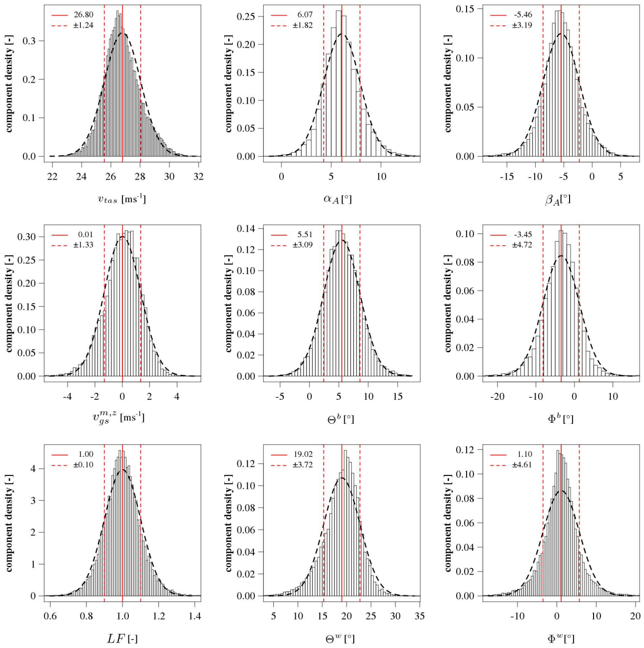

Fig. 4. Histograms of aircraft properties derived from ≈ 3×10^4 data points sampled ≈ 50 m a.g.l. at 10 Hz during the variance optimization flight on 31 July 2009 (Table 3). Component density is scaled so that the histograms have a total area of one. Red vertical lines indicate distribution average (solid) and standard deviation (dashed). The black dashed bell curve displays a reference normal distribution: True airspeed (v_{tas}), attack angle (α_{A}), sideslip angle (β_{A}), aircraft vertical velocity ($v_{\text{gs}}^{\text{m},z}$), trike pitch- ($\Theta^{\text{b}}$) and roll ($\Phi^{\text{b}}$) angles, loading factor (*LF*, the ratio of lift-to weight force), as well as wing pitch- (Θ^{w}) and roll (Φ^{w}) angles.

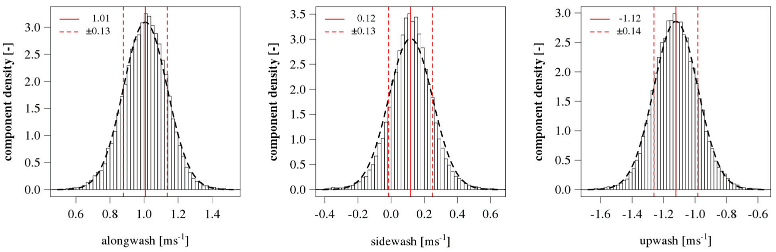

Fig. 5. Histograms of wing-generated alongwash, sidewash and upwash at the five hole probe location. Results are calculated from wing properties in Eqs. (1)–(3) and then rotated from wing- into trike body coordinates (Fig. 3) using Eq. (A13). Presented is the same dataset and in the same manner as in Fig. 4.

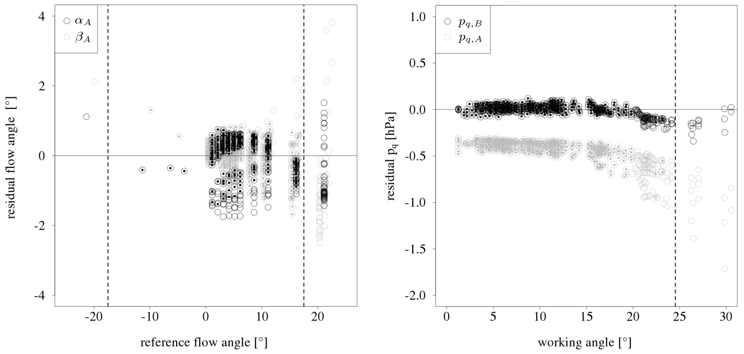

Fig. 6. Wind tunnel evaluation results for true airspeeds from 20 to 32 $\mathrm{m\,s^{-1}}$: open circles represent the residuals for all combinations of flow angles (α_A, β_A, left) and dynamic pressure before ($p_{q,A}$) and after ($p_{q,B}$) wind tunnel correction (right). Full circles indicate subsets that lie in the (extended) operational flow angle range of ±17.5°. These subsets are used for the uncertainty assessment. Dashed vertical lines indicate the corresponding thresholds of flow angle and working angle (acos(cosαcosβ)), respectively.

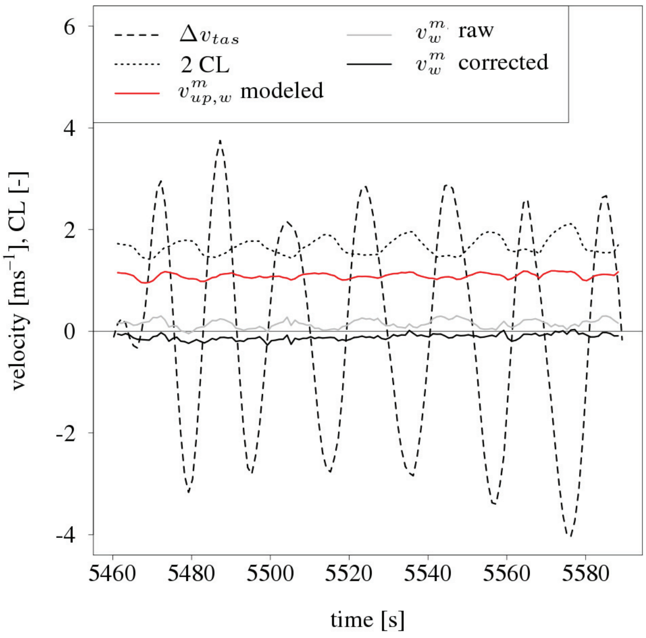

Fig. 7. Forced oscillation pattern (VW3) on 25 June 2008: for improved legibility the average is subtracted from true airspeed (Δv_{tas}) and lift coefficient is inflated by the factor two (2 *CL*). Displayed is the vertical wind ($v_{\mathrm{w}}^{\mathrm{m}}$) before (raw) and after (corrected) correction for dependence on the lift coefficient. For comparison the modelled upwash ($v_{\mathrm{up,w}}^{\mathrm{m}}$) is presented, which was computed using Eq. (3) and decomposed and rotated from wing- into meteorological coordinates using Eq. (A13).

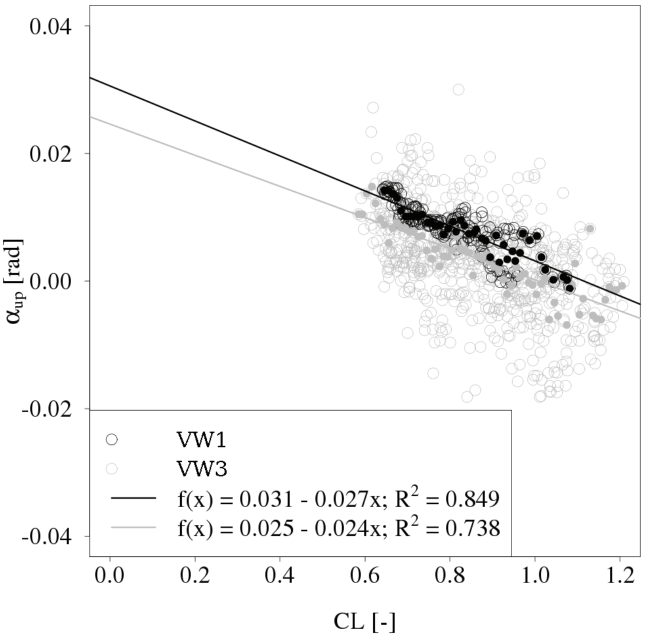

Fig. 8. Upwash angle (α_{up}) as function of the lift coefficient (*CL*) for two vertical wind specific flight patterns: level acceleration-deceleration (VW1) flight and forced oscillation (VW3) flight (both on 25 June 2008). α_{up} is the difference of measured attack angle as measured by the five hole probe, and an inverse reference of the free airstream attack angle. Open circles depict the entire 1 Hz dataset, whereas full circles are averages after binning over increments of 0.01 *CL*.

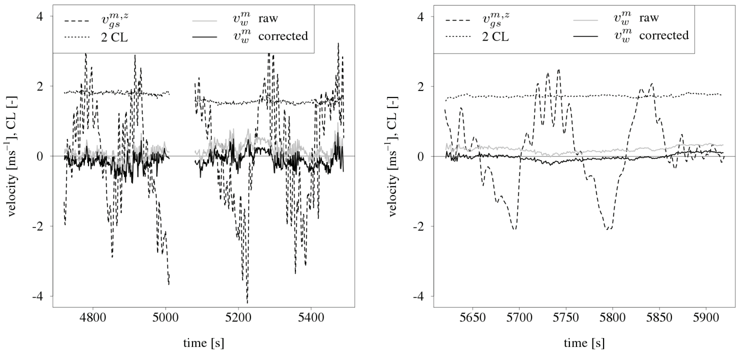

Fig. 9. Smooth oscillation flights (VW2) on 24 June 2008 (left) and 25 June 2008 (right). In addition to the variables explained in Fig. 7 the vertical aircraft velocity ($v_{\mathrm{gs}}^{\mathrm{m},z}$) is shown. The pattern on 24 June 2008 is first carried out at 26 m s^{-1} (4800–5000 s), then at 28 m s^{-1} (5200–5400 s) true airspeed in a less calm airmass. The flight on 25 June 2008 is only conducted at 28 m s^{-1} true airspeed in a calm airmass.

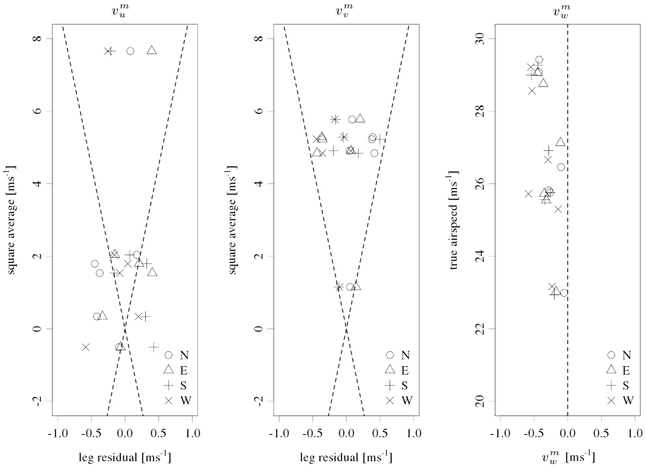

Fig. 10. Results from the wind square flights. For the horizontal wind components ($v_{\mathrm{uv}}^{\mathrm{m}}$) the *x*-axis displays the residuals (leg average – square average), while the *y*-axis shows the wind magnitude. In contrast the vertical wind component ($v_{\mathrm{w}}^{\mathrm{m}}$) is plotted against the true airspeed. Flight legs are depicted with different symbols according to their position in the square pattern. Dashed lines indicate a 10% criteria for $v_{\mathrm{uv}}^{\mathrm{m}}$, and the zero line for $v_{\mathrm{w}}^{\mathrm{m}}$.

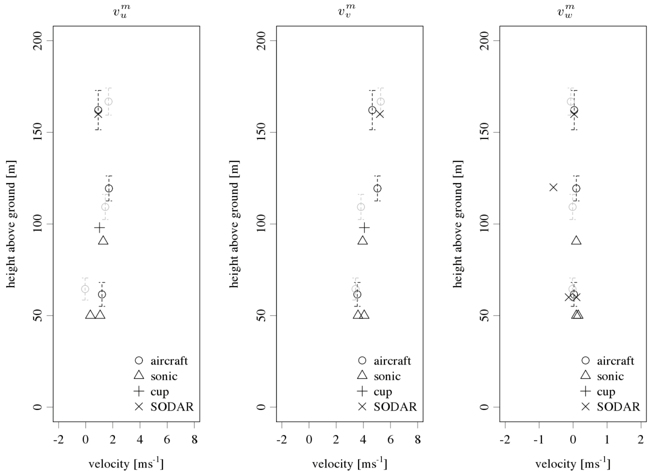

Fig. 11. Vertical profiles for horizontal (v_{uv}^{m}) and vertical (v_{w}^{m}) wind components of simultaneous ground based and weight-shift microlight aircraft measurements on 15 October 2008, 14:50–16:00 CET. Different symbols indicate the different wind sensors. Black circles represent aircraft measurements at 24 m s^{-1} true airspeed, while grey circles represent measurements at 27 m s^{-1} true airspeed. Vertical error bars indicate one standard deviation of the aircraft altitude.

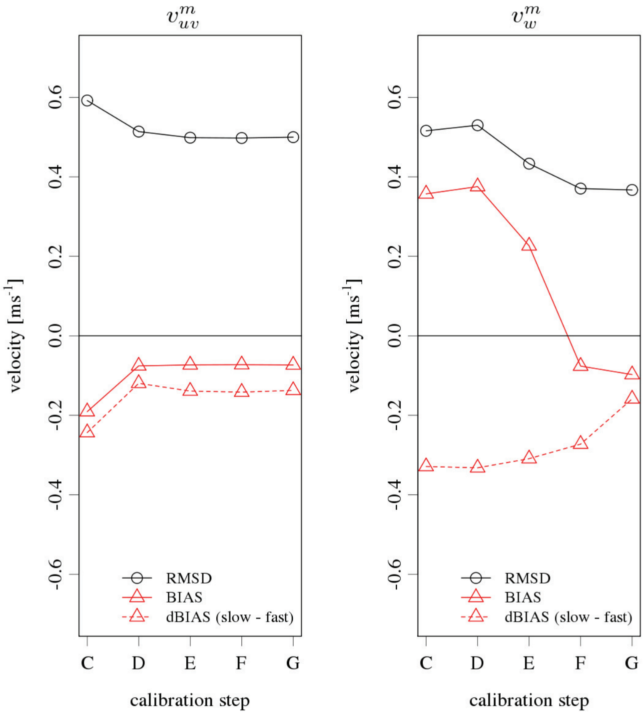

Fig. 12. Influence of the calibration steps C–G on root mean square deviation (RMSD) and bias (BIAS) between weight-shift microlight aircraft and all simultaneous ground based measurements of the horizontal (v_{uv}^{m}) and the vertical (v_{w}^{m}) wind components. dBIAS indicates the difference in BIAS between measurements at 27 and 24 m s^{-1} true airspeed.